

## Research Article

# Study on Modal Dynamic Response and Hydrodynamic Added Mass of Water-Surrounded Hollow Bridge Pier with Pile Foundation

Yulin Deng ,<sup>1</sup> Qingkang Guo ,<sup>2</sup> Yasir Ibrahim Shah ,<sup>3</sup> and Lueqin Xu ,<sup>4</sup>

<sup>1</sup>Associate Professor, Department of Road and Bridge Engineering, Wuhan University of Technology, Wuhan 430063, China

<sup>2</sup>M.S. Candidate, Department of Road and Bridge Engineering, Wuhan University of Technology, Wuhan 430063, China

<sup>3</sup>Ph.D. Candidate, Department of Road and Bridge Engineering, Wuhan University of Technology, Wuhan 430063, China

<sup>4</sup>Associate Professor, Department of Civil Engineering, Chongqing Jiaotong University, Chongqing 400074, China

Correspondence should be addressed to Yulin Deng; [dengyulin@whut.edu.cn](mailto:dengyulin@whut.edu.cn)

Received 27 March 2018; Revised 27 September 2018; Accepted 10 December 2018; Published 6 January 2019

Academic Editor: Fabrizio Paolacci

Copyright © 2019 Yulin Deng et al. This is an open access article distributed under the Creative Commons Attribution License, which permits unrestricted use, distribution, and reproduction in any medium, provided the original work is properly cited.

This article presents an experiment program conducted to study the modal dynamic response of hollow bridge pier with pile foundation submerged in water. The forced vibration method was applied on a specimen designated with four levels of tip mass; and the dynamic characteristics of the first four lateral vibration modes of the specimen, including the first two modes along the  $x$ -axis and the first two modes along the  $y$ -axis, were tested for three different cases where the specimen contacts with only outer water, only inner water, and both outer and inner water, respectively. Finite element models were established using potential-based fluid elements in accordance with the three different cases. The effects of fluid-structure interaction on the dynamic characteristics of the first four lateral modes of the specimen were then investigated through numerical simulations, and the finite element models were verified by validating numerical results against the experimental data. Based on the verified models, hydrodynamic added mass (HAM) and modal hydrodynamic added mass (MHAM) along the  $x$ -axis and  $y$ -axis of the specimen, induced by fluid-structure interaction, were studied with respect to the three cases. According to the distribution of modal acceleration and hydrodynamic pressure along the pier body, hydrodynamic added mass (HAM) distribution along the pier body was analyzed, and a simplified analytical model which equals the original fluid-structure numerical model was proposed to determine the dynamic characteristics of hollow bridge piers submerged in water. The research provides a better understanding of the effect of fluid-structure interaction on the modal dynamic response of deep-water bridges with hollow piers.

## 1. Introduction

Long-span bridges with high piers, such as the Miaoziping Bridge [1, 2], the Sutong Bridge [3, 4], and the China East Sea Bridge [5], are sound solutions for crossing deep-water rivers, reservoirs, straits, and so on. Generally, the high piers are built with voided sections for the sake of structural efficiency and low cost. The bridge substructures are usually composed of a group of piles connected by a large concrete pile cap and a hollow pier body which is usually topped by a cap beam. During the service life of deep-water bridges, the substructures are constantly submerged in deep water, which induces additional force on the structures when

exposed to various dynamic loads, like seismic excitations. The cause of the additional force is the fluid-structure interaction which has long been deemed as an important factor to be considered particularly in seismic design of dams, offshore platforms, and wind farms. It is worthwhile to mention that during the 2008 Wenchuan Earthquake, the Miaoziping Bridge, a typical large-span deep-water bridge with high and hollow piers, suffered severe damage and the fluid-structure interaction between the oscillating piers and surrounding water has been regarded as a crucial trigger [1, 2].

Until recently, analytical approaches to solve the fluid-structure interaction problem fall approximately into two

categories: one is the semianalytical and seminumerical approach and the other is the numerical approach. In the former one, theoretical derivation is performed to obtain analytical formulations for the hydrodynamic pressure which are then applied to the finite element models of structures to account for the fluid-structure interaction, hence the analytical formulations are of utmost importance to the prediction accuracy. Two methods are widely used to formulate the hydrodynamic pressure of cylindrical structures surrounded by water: (1) a method based on the Morison equation or modified Morison equation [6–11]; (2) a method based on the radiation wave theory [12–15]. The semianalytical and seminumerical approach has advantages of both analytical formulation and numerical simulation and hence is widely used to predict the effects of fluid-structure interaction. Currently available formulations for the hydrodynamic pressure, however, still remain to be improved. For example, the method based on the Morison equation is semitheoretical and semiempirical, and the inertia coefficient and drag coefficient defined in the equation are difficult to determine precisely. Moreover, the method cannot be used to take into consideration the effect of inner water inside a hollow structure. Another example, the method based on radiation wave theory is an analytical solution with rigorous theoretical derivation and is applicable when the influence of water compressibility and surface waves should be taken into account, but its formulations are very complicated and inconvenient for practical application. Besides, the method applies only to cylindrical structures with uniform cross section, and therefore it is inappropriate for high and hollow piers whose cross sections usually vary along the height in practical engineering. With technological innovations in engineering computation, numerical methods, such as finite element method and boundary element method, are referred more and more frequently as a solution to the dynamic response of fluid-structure interaction [16–22]. But the numerical models are usually complicated with a huge number of elements, and the solutions are computationally inefficient. Furthermore, the numerical methods cannot account accurately for the nonlinearities such as structural damage, concrete cracking, and so on.

To validate the theoretical and numerical methods, some experiments have been conducted to study fluid-structure interaction and supportive test data have been obtained [20, 23–27]. It can be found that most of these experiments were conducted on cantilever columns, towers, and other cylindrical structures with solid cross sections. But in this study, an experimental program was designed to investigate the dynamic responses of a high and hollow bridge pier submerged in deep water. During the study, the first two lateral vibration modes along the  $x$ -axis and  $y$ -axis of the specimen were tested in various combined conditions of water levels and tip masses. The tests were conducted for three cases where the specimen contacts with only outer water, only inner water, and both outer and inner water. Using potential-based fluid elements, 3D finite element models were established for each case and each condition. The numerical models were verified since the

numerical results were successfully validated against the obtained test data. Based on the verified models, the hydrodynamic added mass (HAM) and the modal hydrodynamic added mass (MHAM) along the  $x$ -axis and  $y$ -axis of the specimen were studied from the three cases, respectively. According to the distribution of hydrodynamic added mass (HAM) along the specimen, the equivalent analytical model was finally proposed for calculating the dynamic characteristics of hollow bridge piers surrounded by water.

## 2. Experimental Program

**2.1. Selection of Similarity Ratio.** A specimen was designed based on a reduced scale. During dynamic similarity ratio design, the inertial force, the gravity, and the restoring force of the specimen need to satisfy the equation written as

$$\frac{S_E}{S_g S_\rho} = S_I, \quad (1)$$

where  $S_E$  is the similarity constant of the elastic modulus;  $S_g$  is the similarity constant of the gravitational acceleration;  $S_\rho$  is the similarity constant of the density; and  $S_I$  is the similarity constant of the geometrical dimensions. It is important to note that the equation above can hardly be achieved especially for the specimen composed of two materials (reinforced concrete), so the similarity ratio is approximate.

In order to strictly satisfy the similarity ratio between the self inertia force of the structure and the additional inertia force of the water, the similarity constants of the structure density and the water density need to be kept the same. The water used in the tests is the same as the prototype water, so the similarity constant of the structural density  $S_\rho$  is 1. The similarity constant of the gravitational acceleration is also 1. According to the dimensions of the prototype bridge pier and other conditions,  $S_I$  was selected as 1/40 and the actual dimensions of the specimen were adjusted, for example, the pier height of the specimen was adjusted to 1.6 m because the bridge pier is partly submerged in water. The similarity constants of other physical properties needed are listed in Table 1.

**2.2. Design of Test Specimen.** The specimen was inspired by a prototype deep-water bridge with large spans and hollow piers. The prototype is the Miaozi Ping Bridge which is located near the epicenter of the Wenchuan Earthquake, 29 km from Yingxiu town in southwestern China, as schematically shown in Figure 1. The main bridge is a three-span continuous framed bridge with two intermediate hollow piers about 100 m high. The hollow piers, designated as No. 3 pier and No. 4 pier, are submerged in the Zipingpu reservoir to a depth of 50 m. At the time of the Wenchuan Earthquake, the construction of the bridge was almost completed except for the installation of expansion joints. During the earthquake, the intermediate hollow piers suffered severe damage with several penetrating cracks propagating at the bottom of the piers. Figure 2 presents the

TABLE 1: Physical properties of the designed specimen.

Types	Physical quantities	Similarity relations	Values
Material properties	Young's modulus	$S_E$	1/40
	Density	$S_\rho = S_E/S_I$	1
Geometrical properties	Length	$S_I$	1/40
	Linear displacement	$S_x = S_I$	1/40
Dynamic properties	Mass	$S_m = S_\rho S_I^3$	1/64000
	Stiffness	$S_k = S_E S_I$	1/1600
	Time	$S_t = (S_m/S_k)^{1/2}$	$(1/40)^{1/2}$
	Frequency	$S_\omega = 1/S_t$	40 $^{1/2}$

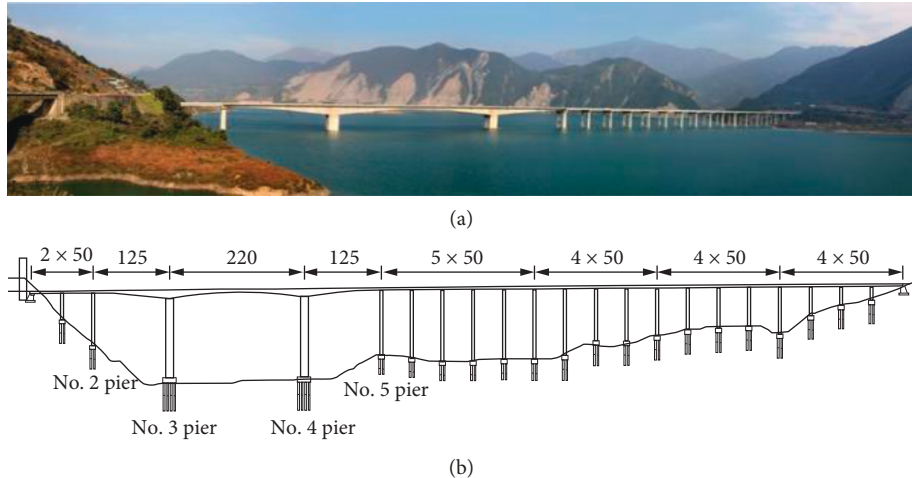


FIGURE 1: General layout of the Miaoziping Bridge; all dimensions are in meters. (a) Picture of the Miaoziping Bridge. (b) Elevation view.

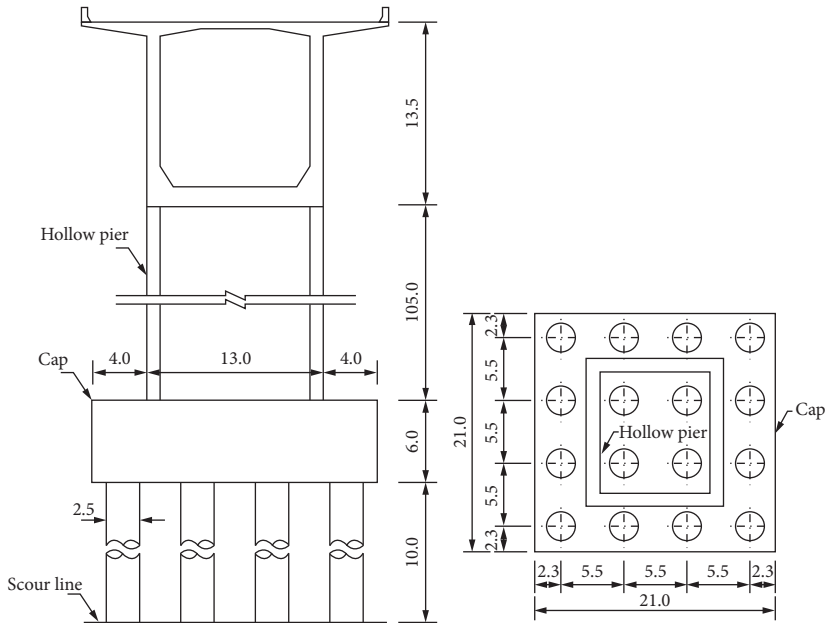


FIGURE 2: Dimensions of the prototype hollow pier; all dimensions are in meters.

dimensions of No. 3 pier, which is composed of 16 piles, a pile cap, and a pier body. The pier body was constructed with Chinese Grade C50 concrete, which has Young's modulus of 34.5 GPa. The piles and cap were constructed with C30

concrete [28], and Young's modulus of C30 concrete is 30 GPa.

As shown in Figure 3, a reduced scale hollow pier specimen was built. The specimen consists of six steel tube

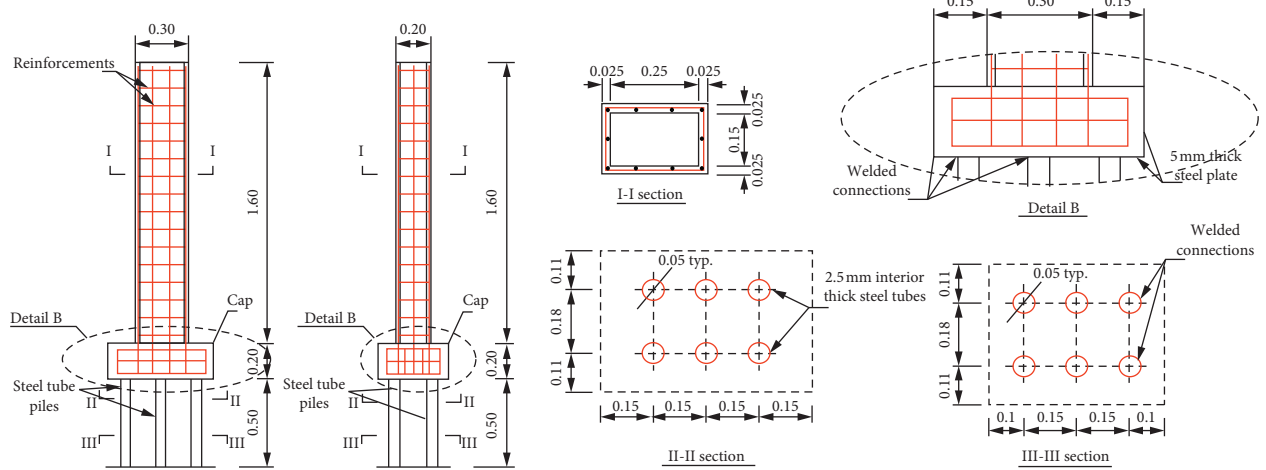


FIGURE 3: Dimensions and details of the hollow pier specimen; all dimensions are in meters unless otherwise specified.

piles, a concrete-filled steel cap, and a reinforced concrete hollow pier body. Steel tubes, 0.05 m in diameter and 2.5 mm in thickness, were used to simulate the concrete piles mainly for ease of construction and safety of loading. The concrete-filled steel box was used to model the pile cap mainly for the reason to ensure a secure connection between the piles and cap. The pile cap is  $0.60 \times 0.40 \times 0.20$  m in dimension, and it consists of two  $0.60 \times 0.20 \times 0.005$  m lateral steel plates in the long side, two  $0.40 \times 0.20 \times 0.005$  m lateral steel plates in the short side, a  $0.60 \times 0.40 \times 0.01$  m steel base plate, and inner cast-in-situ concrete. All the steel plates of the cap have a density of  $7,850 \text{ kg/m}^3$  and Young's modulus of 210 GPa. The steel tube piles were welded at one end to a 5 mm thick steel plate which was fixed on the tank's bottom plate in advance, and the other end of these tubes was welded to the pile cap bottom. The hollow pier body is 1.6 m in height, with a single-cell cross section of  $0.30 \times 0.20 \times 0.025$  m. It is made of C15 concrete according to the Chinese code, with a density of  $2,300 \text{ kg/m}^3$  and Young's modulus of 22 GPa. Young's modulus of the material selected (C15) is smaller than the original material (C50), mainly to guarantee the measurement requirements. The pier body is reinforced by ten Chinese Grade HRB400 longitudinal steel bars and HPB300 [29] stirrups. The bars have a diameter of 8 mm, and the stirrups have a diameter of 6 mm which are placed at a vertical spacing of 0.1 m. It is essential to note that the change rules of the specimen-water interaction as a function of water level were studied in this study and the reduction scale effects will not affect the change rules, and some numerical and experimental analyses can be referred from previous study [30].

**2.3. Instrumentation and Test Procedure.** In this experimental research, a steel water tank was designed and built in advance to create a deepwater environment for the test specimen. The detailed introduction of the water tank (including the size effect analysis), experimental instruments, and experimental method were presented in a previous

study conducted by Deng et al. [30]. Three different cases were considered in the research and designated as case I (where the specimen was in contact with the water only surrounding the outside surfaces of the specimen, or precisely, contact only with outer water), case II (where the specimen interacted with the water only existing inside the hollow pier body, or precisely, interacted only with inner water), and case III (where the specimen was in contact with both outer and inner water). Forced vibration tests were carried out repeatedly to investigate the modal dynamic response of the specimen with different tip masses: (1) surrounded by 16 levels of outer water, varying from 0 to 1.8 m for an empty to full water tank, respectively; (2) interacting with 11 levels of inner water, varying from 0.8 m to 1.8 m (corresponding to a water height of 0.05 m to 1.05 m inside the hollow pier body); (3) contact with both outer and inner water for the same 16 levels of water heights as defined previously. The designed water levels can be seen in Figure 4. The tests for the above three cases were all repeated for a tip mass of 0, 11.4, 23.4, and 31.7 kg, respectively. Various tip masses were used to examine the effect of bridge superstructure mass, and they were imposed at the top of the pier through steel bricks.

A small hole was drilled at the bottom of the pier body in advance; during the tests for case I and case II, the hole was plugged through viscose rayon so that these two cases could be conducted separately. After the tests for case II were successfully performed, the hole was released and the water inside the hollow pier body was poured out. Then, the tests for case III could be conducted, and due to the hole, the water levels inside and outside the hollow pier body were purposely kept the same.

### 3. Numerical Simulations

**3.1. Fluid-Structure Interaction Formulation.** In a fluid-structure system, the vibration of structure induces water flow normal to the structural boundaries which produces additional hydrodynamic pressure acting on the structure. The well-known  $\phi - U$  formulation can be used to represent

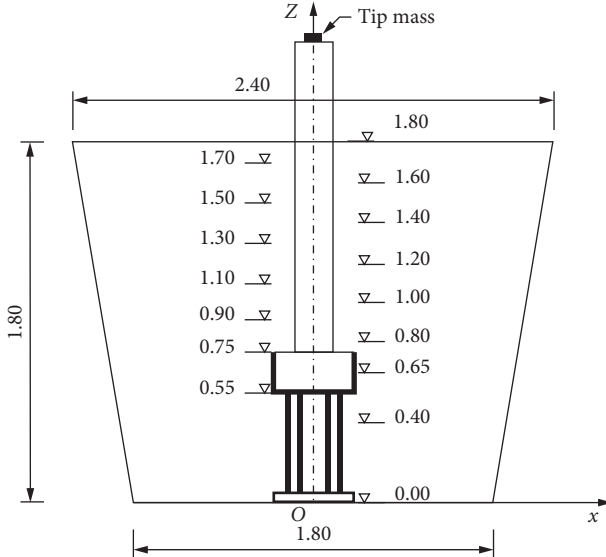


FIGURE 4: Water levels considered during the tests; all dimensions are in meters.

the procedure of fluid-structure interaction, and the corresponding fluid element is the potential-based fluid element. In the  $\phi-U$  formulation,  $U$ , representative of displacement, is used as a static variable in the solid domain and  $\phi$ , representative of velocity potential, is used in the fluid domain. The potential-based fluid element is assumed to be in viscous, irrotational, compressible, or almost incompressible (slightly compressible), with no heat transfer and relatively small displacements on the fluid-structure boundaries. The potential-based fluid element has been proved to be reliable and computationally efficient and has been widely applied in modeling the water-surrounded dams, cylinders, towers, and so on [16, 18, 19, 31]. So, it is adopted in this work. According to the potential-based fluid theory, the wave equation is written as

$$\nabla^2 \phi = \left( \frac{1}{C_w^2} \right) \left( \frac{\partial^2 \phi}{\partial t^2} \right), \quad (2)$$

where  $C_w$  is velocity of compressive waves within water and  $t$  is time variable. In order to solve equation (2) with respect to a hollow bridge pier with pile foundation, the following boundary conditions are specified for the velocity potential  $\phi$ :

- (i) An essential boundary condition at the free surface and the four lateral and bottom rigid walls of the water tank:

$$\phi = 0. \quad (3)$$

- (ii) A natural boundary condition at fluid-structure interfaces, including the water-piles, water-cap, and water-pier body interfaces:

$$\frac{\partial \phi}{\partial n} = \dot{u}_n, \quad (4)$$

where  $\dot{u}_n$  is positive normal velocity corresponding to unit surface normal vector and  $n$  pointing into the water tank out of the structure.

Equation (2) can be derived through standard techniques and discretized to obtain the following nonstandard eigenvalue problem:

$$\left( -\omega_j^2 \begin{bmatrix} \mathbf{M} & \mathbf{0} \\ \mathbf{0} & \mathbf{M}_{FF} \end{bmatrix} - \omega_j \begin{bmatrix} \mathbf{0} & \mathbf{C}_{FU}^T \\ \mathbf{C}_{FU} & \mathbf{0} \end{bmatrix} + \begin{bmatrix} \mathbf{K} + (\mathbf{K}_{UU})_S & \mathbf{0} \\ \mathbf{0} & \mathbf{K}_{FF} \end{bmatrix} \right) \cdot \begin{bmatrix} \mathbf{U}^{(j)} \\ \mathbf{F}^{(j)} \end{bmatrix} = \begin{bmatrix} \mathbf{0} \\ \mathbf{0} \end{bmatrix}, \quad (5)$$

where  $\mathbf{F}^{(j)} = -i\phi^{(j)}$  in which  $i = \sqrt{-1}$  and  $\phi^{(j)}$  is fluid potential eigenvector;  $\mathbf{U}^{(j)}$  is modal displacement eigenvector in which  $\mathbf{M}$  is structural mass matrix;  $\mathbf{M}_{FF}$  is potential energy matrix of water domain;  $\mathbf{C}_{FU}$  is matrix coupling the velocity potential to displacements on the fluid-structure interfaces;  $\mathbf{K}$  is structural stiffness matrix;  $\mathbf{K}_{FF}$  is the kinetic energy matrix for water;  $(\mathbf{K}_{UU})_S$  is the matrix relating to the structural stiffness to water motion; and  $\omega_j$  is coupled frequency of water-structure system along mode  $j$ .

Equation (5) is a nonstandard eigenvalue problem in which all of the eigenvalues are real and nonnegative. It can be solved using either the Determinant search method or the Lanczos iteration method.

**3.2. Finite Element Models.** Generally, the potential-based finite elements have been used in numerical simulations. The purpose is to compare the results obtained experimentally and numerically, respectively, and to validate the numerical procedures used widely to explore the dynamic characteristics of fluid-structure interaction.

Three-dimensional (3D) finite-element models are established using the finite element code ADINA [31] to model the tested hollow pier specimen and water. As illustrated in Figure 5, the 3D 8-node shell finite elements available in ADINA are used to model the steel tube piles, and the 3D 20-node solid finite elements are used to model the rest of the specimen including the pier body and pile cap. The tip mass is represented by the concentrated mass elements, and the water domains, including outer water and inner water, are meshed using the 3D 20-node potential-based fluid elements. The ADINA code provides a convenient function to generate automatically fluid-structure interface elements along the boundaries between the fluid and structure. The bounding surfaces of the water domain are modeled using various types of potential interfaces, like free surface, fluid-structure interface, and rigid wall. Fluid-structure interaction is accounted for through these potential interfaces defined at the water-structure interfaces. The physical properties of the tested hollow pier specimen and water are listed in Table 2.

For each value of the tip mass, finite-element models were established for the dry structure, i.e., without water, and the wet structures submerged by 15 water levels in case I and III, and by 11 inner water levels in case II, as shown in Figure 4. This resulted in a total of 168 finite-element models with 42 for each of the four tip masses.

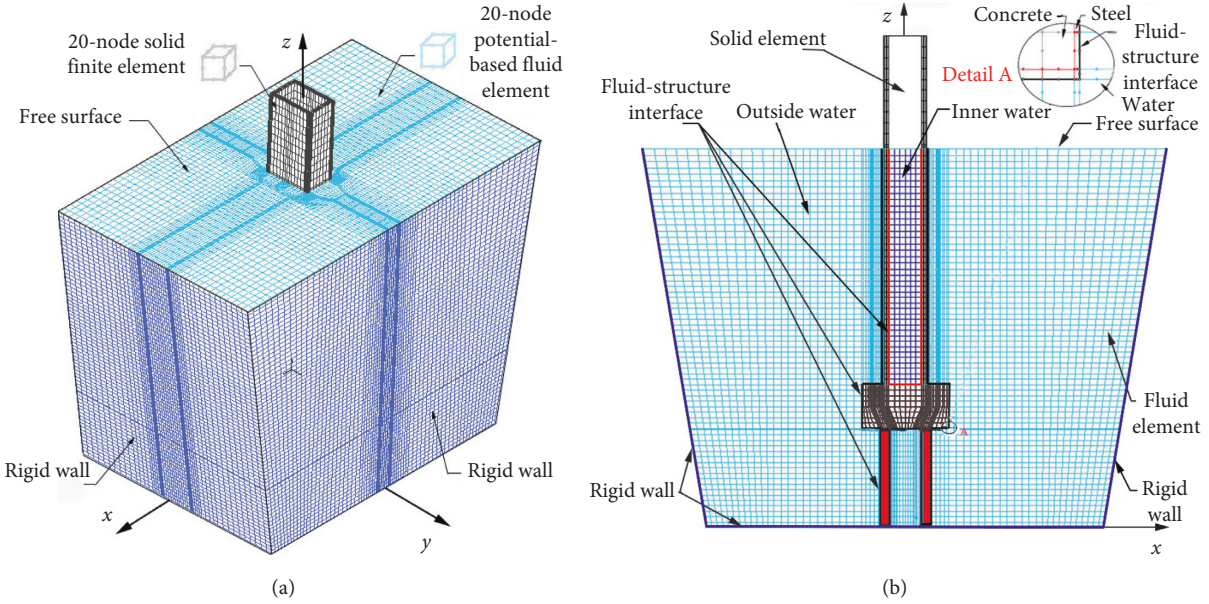


FIGURE 5: Finite-element model of the hollow pier specimen and water domain: (a) overview; (b) elevation view through a central cutting plane.

TABLE 2: Material properties.

Material	Elasticity modulus	Mass density	Poisson ratio	Velocity of compression waves
Concrete	$E_c = 22 \text{ GPa}$	$\rho_c = 2,300 \text{ kg/m}^3$	$\nu_c = 0.2$	\
Steel	$E_s = 210 \text{ GPa}$	$\rho_s = 7,830 \text{ kg/m}^3$	$\nu_s = 0.3$	\
Water	\	$\rho_w = 1,000 \text{ kg/m}^3$	\	$C_w = 1,440 \text{ m/s}$

#### 4. Comparison and Discussion of Experimental and Numerical Results

**4.1. Definition of the Vibration Period Increase Rate.** In order to discuss the effect of fluid-structure interaction on the modal dynamic response of the specimen, vibration period increase rate is defined herein to show the tendency of the specimen vibration period in different test cases. The vibration periods  $T_{xj}^0$  and  $T_{yj}^0$ ,  $j = 1, 2$ , are the results of the specimen without water, corresponding to the first two modes along the  $x$ -axis and  $y$ -axis, respectively. The vibration periods  $T_{xj}^w$ ,  $j = 1, 2$ , and  $T_{yj}^w$ ,  $j = 1, 2$ , correspond to the first two modes along the  $x$ -axis and  $y$ -axis, respectively, which were determined for each water level considered in this paper. The vibration period increase rates  $\text{Inc}T_{xj} = (T_{xj}^w - T_{xj}^0)/T_{xj}^0$  and  $\text{Inc}T_{yj} = (T_{yj}^w - T_{yj}^0)/T_{yj}^0$ ,  $j = 1, 2$  were then obtained for each tip mass.

During this study, higher orders of mode are not easy to be excited in a steady condition based on traditional forced vibration tests, and they were not the major concern of this experimental research. The torsional mode was not taken into consideration during the tests, because in most cases the torsional mode contributes little to the seismic response of bridges, especially to that of straight bridges.

**4.2. Effect of Outer Water-Structure Interaction on Vibration Periods.** In case I, only the water surrounding the outer

surfaces of the specimen was considered during the tests with a purpose of investigating the effect of outer water-structure interaction on the hydrodynamic modal response of the specimen. Figure 6 presents the trends of the periodical percentage increases of the specimen with respect to the outer water level changing from 0 to 1.8 m, for an empty to full water tank, for the four tip masses, respectively. Along with the experimental (EXP) results, the numerical results (FEM) obtained using the finite-element models described previously are also given in these figures.

As shown in these figures, a satisfactory agreement is displayed between the numerical results and the experimental data for all combinations of water level and tip mass. It can be revealed that (1) when the water level is below the pile cap, i.e.,  $H_w < 55 \text{ cm}$ , the period percentage increases of the four lateral modes remain practically constant under the four tip masses, implying that the hydrodynamic effect of water-piles interaction is negligibly weak when bridges are submerged by water up to the bottom of pile caps; (2) when the water level is just over the entire height of the pile cap, i.e.,  $55 \text{ cm} < H_w < 75 \text{ cm}$ , the curves of the four lateral modes under the four tip masses ascend obviously but limitedly, indicating that the fluid-structure interaction between water and pile cap plays an more important role in the hydrodynamic response of the specimen than that of between water and piles; (3) and when the pier body is submerged in water, i.e.,  $H_w > 75 \text{ cm}$ , a continuous rise of the curves can be

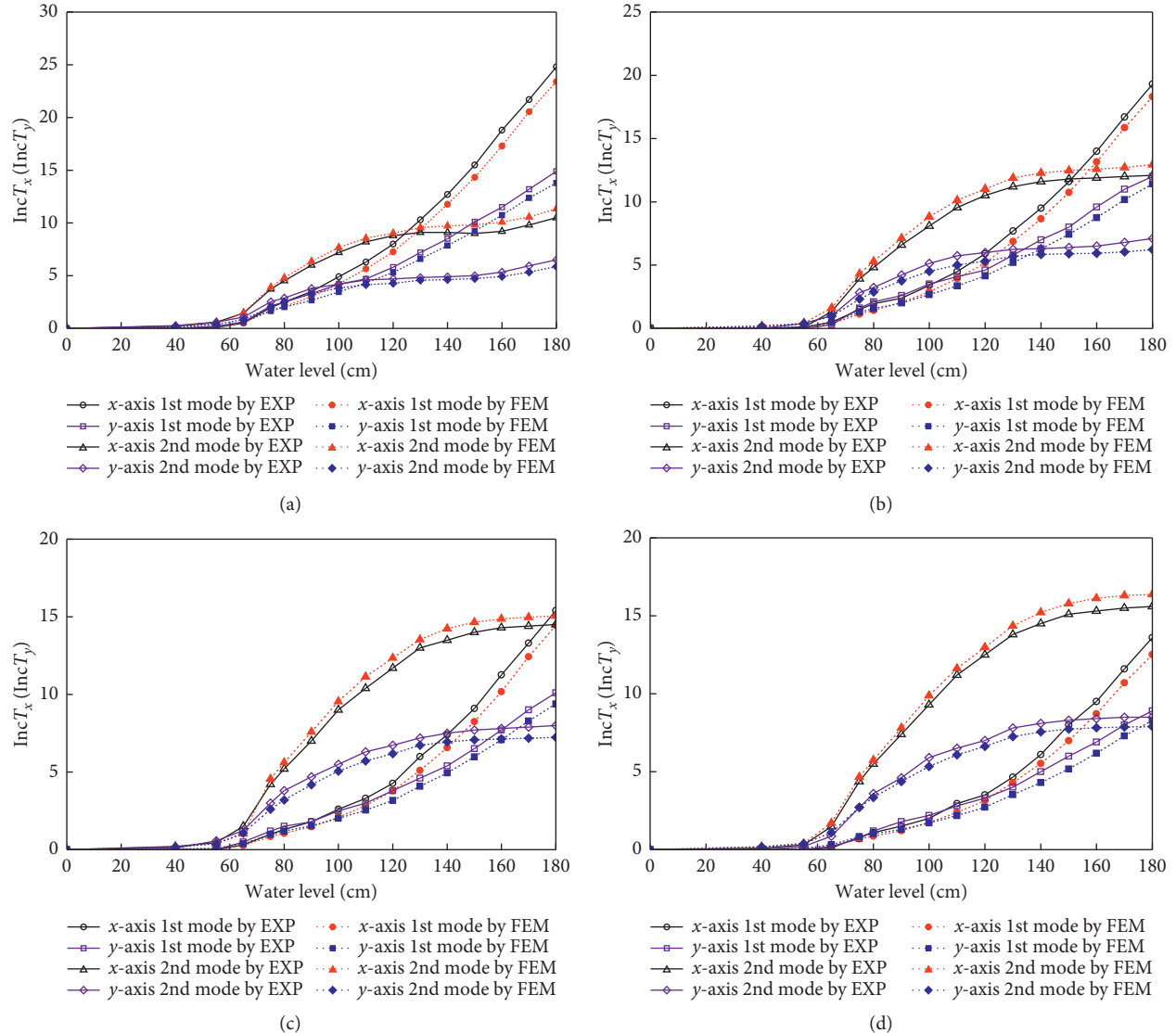


FIGURE 6: Measured and computed percentage increases of vibration period for the hollow pier specimen in case I as a function of water level: (a) without tip mass; (b) with an 11.4 kg tip mass; (c) with a 23.4 kg tip mass; and (d) with a 31.7 kg tip mass.

observed in the four lateral modes under the four tip masses, especially in those along the  $x$ -axis due to the fact that the area of fluid-structure potential interfaces perpendicular to the  $x$ -axis is larger than that perpendicular to the  $y$ -axis. Besides, the figures also reveal a different trend between the results of first lateral modes and second lateral modes for the four tip mass cases. With the increase of water levels, the period percentage increases for the second modes grow quickly in the beginning and then in a much slower pattern, whereas the period percentage increases for the first modes grow contrarily.

It is important to note that the maximum period percentage increases are approximately 23% for the first lateral modes and about 15% for the second lateral modes along the  $x$ -axis, both occurring when the water tank is full. Therefore, it might be neoconservative to overlook the hydrodynamic loads in design and construction of bridges with hollow piers submerged in deep water.

#### 4.3. Effect of Inner Water-Structure Interaction on Vibration Periods.

Since small holes, intentionally reserved for construction purposes, are commonly found in reinforced concrete piers, it is not difficult to accept that the hollow chambers of pier body could be filled with water when it is submerged in deep water. It is necessary to point out that case II where the bridge interacts only with the water inside its hollow piers is not common in practical engineering, but it is still of a certain significance in understanding the hydrodynamic behavior of hollow structures. Figure 7 illustrates the trends of the period percentage increases of the specimen with respect to the inner water level changing from 0.8 to 1.8 m for the four tip masses, respectively. For the sake of comparison, the abscissas of the figures still start from 0 to 180 cm, from which the ranges of 0–80 cm correspond to the results obtained using dry specimen (the specimen without water).

Figure 7 manifests a sound agreement between the numerical results and test data for all considered cases. It can

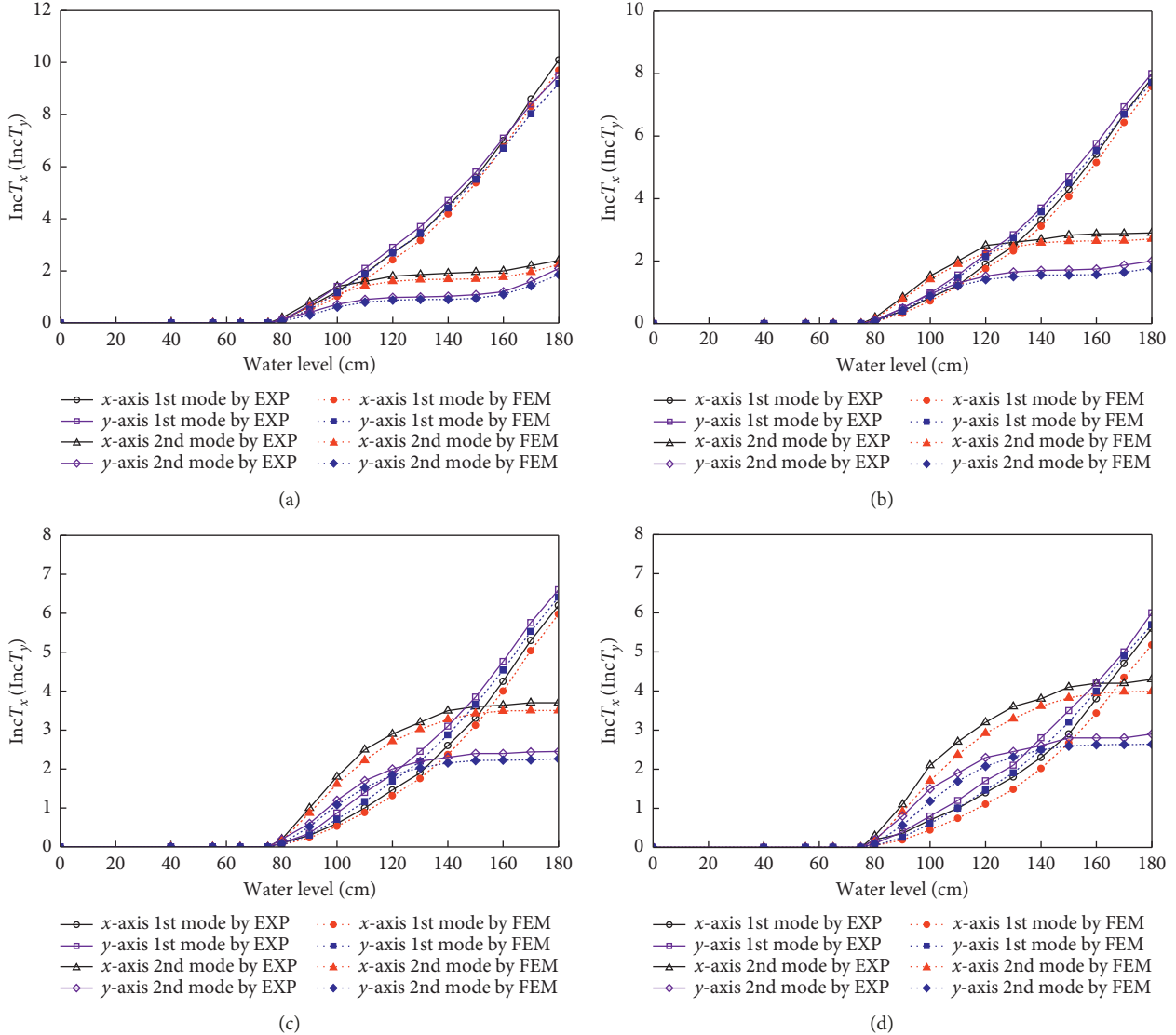


FIGURE 7: Measured and computed percentage increases of vibration period for the hollow pier specimen in case II as a function of water level: (a) without tip mass; (b) with an 11.4 kg tip mass; (c) with a 23.4 kg tip mass; and (d) with a 31.7 kg tip mass.

be seen that the vibration periods of the specimen become larger as the water level increases, indicating that the effect of fluid-structure interaction is more remarkable with increasing water level. It is not surprising that similar observations can be made in case II just as in case I. But a discrepancy can still be noticed that in case II: the results along the  $x$ -axis are closer to those along the  $y$ -axis. Similar to the trends in case I, the period percentage increases for the first modes for both directions in case II decrease when the tip mass becomes larger, whereas the period percentage increases of the second modes show an opposite tendency. By comparison between Figures 6 and 7, it can be found that the effect of inner water-structure interaction is not that notable when compared with outer water-structure interaction, and in case II, the maximum period percentage increases are approximately 10% for the first lateral modes and about 4% for the second lateral modes.

**4.4. Effect of Water-Structure Interaction on Vibration Periods Taking into Consideration Both Outer and Inner Water.** The period percentage increases of the specimen with respect to the outer water level are shown in Figure 8 for the four tip masses, respectively. A satisfactory agreement can also be found between the numerical results and experimental data for all considered combinations of water level and tip mass. For the same lateral mode, the variation trends of the period percentage increases with the water level and tip mass are closer to those observed in case I; this provides further evidence that the effect of outer water plays a dominant part. It is worthwhile to point out that the period percentage increases for the four lateral modes in case III are the largest among the three considered cases. For example, the period percentage increases reach a maximum of about 30% for the first lateral mode and nearly 20% for the second lateral mode.

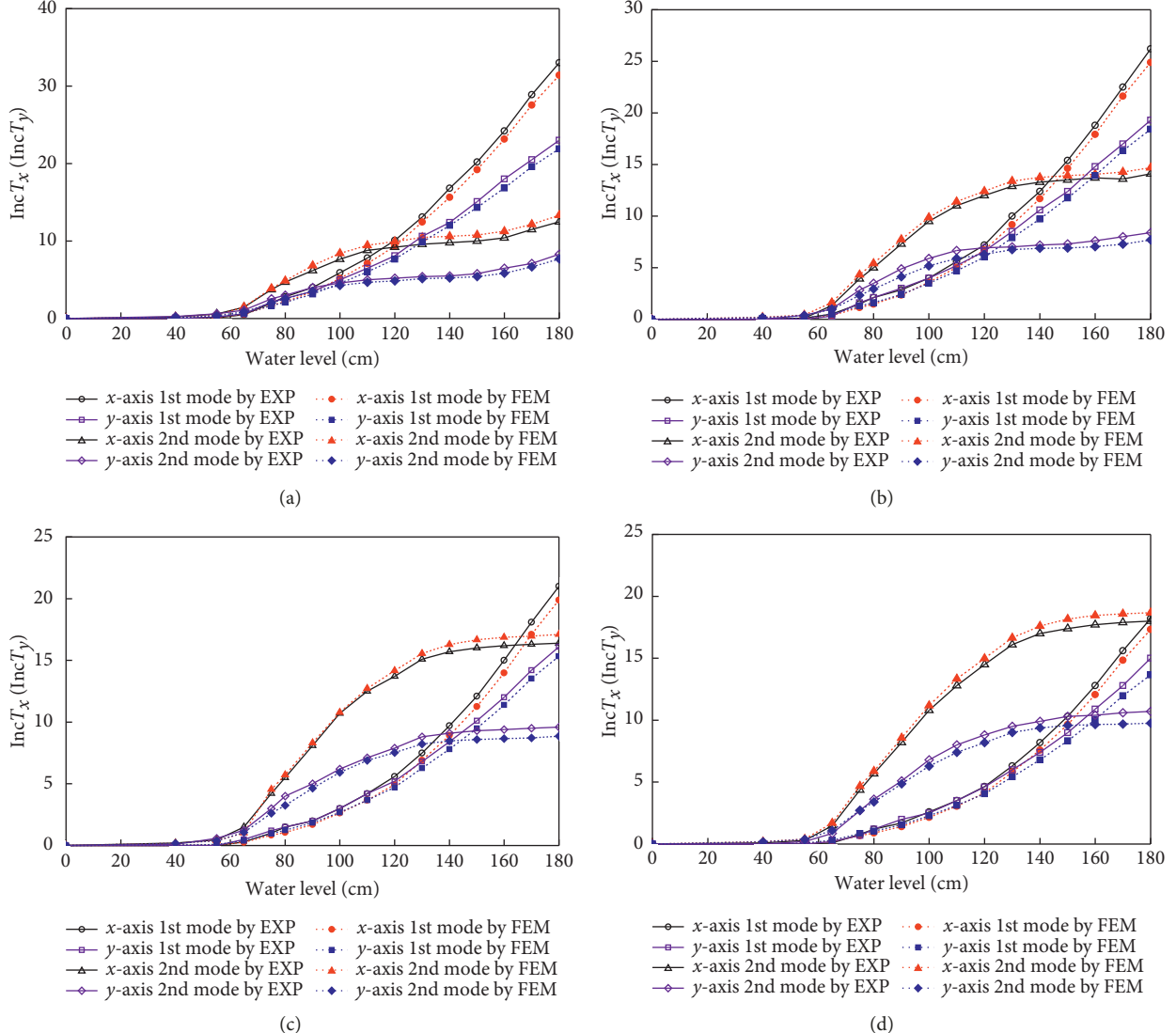


FIGURE 8: Measured and computed percentage increases of vibration period for the hollow pier specimen in case III as a function of water level: (a) without tip mass; (b) with an 11.4 kg tip mass; (c) with a 23.4 kg tip mass; and (d) with a 31.7 kg tip mass.

**4.5. Effect of the Added Mass.** It is validated that the experimental results and the numerical results are in good agreement under different cases and tip masses. And the curve trends in case III are similar to those in case I, which indicate that the outer water plays a dominant part in affecting structural dynamic properties. Hence, in this section, only the computed period percentage increases (FEM results) as a function of water level for each vibration mode and tip mass under case I and case III are shown in Figure 9. It is interesting to notice that, under both cases, the period percentage increases of the first modes for both directions decrease when the tip mass becomes larger, whereas the period percentage increases of the second modes show an opposite trend. It is implied that the effect of fluid-structure interaction is attenuated in the first modes but strengthened in higher order modes as the tip mass increases. The same trends can be found in case II which is not presented here. It is also indicated from each plot of Figure 9 that the effect of fluid-structure interaction in case III is always greater than

that in case I for each water level and tip mass, because of the existence of inner water in case III.

## 5. Hydrodynamic Added Mass

**5.1. Modal Participation Mass of Fluid-Structure System.** Both experimental and numerical results revealed that the vibration period increase is noticeable when the specimen is submerged in water (or interacts with inner water). Generally, it is accepted that, in water-structure interaction system, water has little impact on the stiffness of structure and the additional damping of the system induced by water, can be neglected, and therefore the main factor leading to the increase of vibration periods is attributed to the hydrodynamic added mass [11, 12, 24]. Several formulations for the hydrodynamic added mass have been proposed by means of theoretical derivation during past decades [12, 14, 32], but the formulations have been derived based on column structures with a uniform circular or rectangular cross

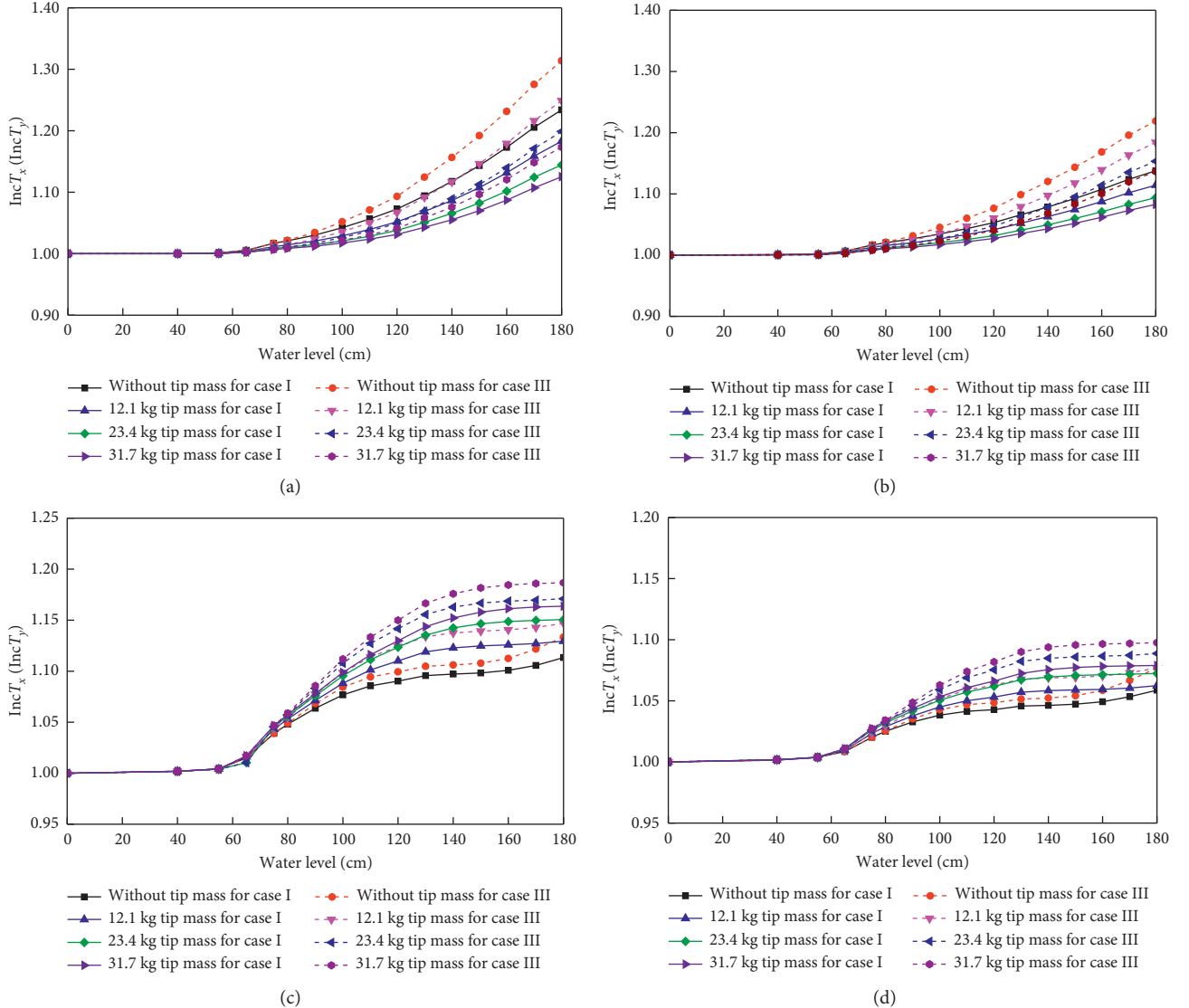


FIGURE 9: Computed period percentage increases for the pier specimen as a function of water level: (a) first mode along the  $x$ -axis; (b) first mode along the  $y$ -axis; (c) second mode along the  $x$ -axis; and (d) second mode along the  $y$ -axis.

section. As for the hollow pier investigated herein, it might be difficult to derive a theoretical formulation for the hydrodynamic added mass. With technological competence of numerical methods in computing the problem of fluid-structure interaction, the hydrodynamic added mass for complex structures can be obtained through numerical simulations [16, 31, 33].

In a water-structure system, the modal participation mass for each vibration mode consists of two sources: one originating from the structural participation mass and the other from hydrodynamic added mass [33]. In a specific direction, the hydrodynamic added mass for each water level can be obtained through subtraction of the accumulated modal participation masses between the water-structure system and dry-structure system, as presented in detail in Section 5.2. The principle and procedure for determining the modal participation mass of water-structure system can be found in ADINA [31]; and they are briefly introduced below.

The motion equation of a fluid-structure interaction system under ground motion loading is given as follows:

$$\begin{bmatrix} \mathbf{M} & \mathbf{0} \\ \mathbf{0} & \mathbf{M}_{FF} \end{bmatrix} \begin{bmatrix} \ddot{\mathbf{U}}_r \\ \ddot{\phi} \end{bmatrix} + \begin{bmatrix} \mathbf{0} & \mathbf{C}_{FU}^T \\ -\mathbf{C}_{FU} & \mathbf{0} \end{bmatrix} \begin{bmatrix} \dot{\mathbf{U}}_r \\ \dot{\phi} \end{bmatrix} + \begin{bmatrix} \mathbf{K} + (\mathbf{K}_{UU})_S & \mathbf{0} \\ \mathbf{0} & \mathbf{K}_{FF} \end{bmatrix} \begin{bmatrix} \mathbf{U}_r \\ \phi \end{bmatrix} = - \begin{bmatrix} (\mathbf{K}_{UU})_S \mathbf{d}_k \\ 0 \end{bmatrix} u_{gk} \quad (6)$$

$$- \begin{bmatrix} \mathbf{M} \mathbf{d}_k \\ -\mathbf{C}_{FU} \mathbf{d}_k \end{bmatrix} \dot{u}_{gk},$$

where  $\mathbf{M}$  is the mass matrix for the system;  $\mathbf{K}$  is the stiffness matrix for the system;  $\mathbf{M}_{FF}$  is the potential energy matrix for water;  $\mathbf{K}_{FF}$  is the kinetic energy matrix for water;  $(\mathbf{K}_{UU})_S$  is the matrix relating the structural stiffness to water motion;  $\mathbf{C}_{FU}$  is the matrix coupling the velocity potential to displacements on the water-structure interfaces;  $\mathbf{U}_r$  is the vector

for nodal displacements with respect to the ground motion;  $\phi$  is the velocity potential corresponding to the absolute (not relative) velocities;  $\dot{u}_{gk}$  is the ground displacements in direction  $k$ ; and  $d_k$  is the vector of nodal point values in which  $d_k(i) = 1$  if equation  $i$  corresponds to a translation in direction  $k$  and  $d_k(i) = 0$  otherwise.

Equation (6) can be solved by mode superposition if the structural damping is neglected, the assumption of infinitesimal velocity is warranted, and no infinite boundaries are defined.

The modal expansions are given in the following:

$$\begin{aligned} \mathbf{U}_r &= \sum_{j=1}^n x_j \mathbf{U}^{(j)}, \\ \dot{\phi} &= \sum_{j=1}^n -\omega_j x_j \mathbf{F}^{(j)}, \end{aligned} \quad (7)$$

where  $x_j$  is generalized coordinate of the  $j$ th mode;  $\omega_j$  is the  $j$ th modal frequency; and  $\mathbf{U}^{(j)}$  and  $\mathbf{F}^{(j)}$  are, respectively, the displacement eigenvector and fluid potential eigenvector of the  $j$ th mode, which can be determined by eigenvalue analysis. Generally, the eigenvectors are scaled according to the following orthogonality condition:

$$\begin{aligned} (\mathbf{u}^{(i)} \mathbf{C}_{FU}^T \mathbf{F}^{(j)}) + (\mathbf{F}^{(i)} \mathbf{C}_{FU} \mathbf{u}^{(j)}) \\ + ((\omega_i + \omega_j)(\mathbf{u}^{(i)} \mathbf{M}_{UU} \mathbf{u}^{(j)} + \mathbf{F}^{(i)} \mathbf{M}_{FF} \mathbf{F}^{(j)})) = 2\sqrt{\omega_i \omega_j} \delta_{ij}, \end{aligned} \quad (8)$$

where  $\delta_{ij}$  is the Kronecker delta,  $\mathbf{u}^{(i)}$  and  $\mathbf{u}^{(j)}$  are the structural displacement vectors for mode  $i$  and  $j$  respectively;  $\mathbf{F}^{(i)}$  and  $\mathbf{F}^{(j)}$  are the fluid plural velocity potentials for mode  $i$  and  $j$  respectively; and  $\omega_i$  and  $\omega_j$  are the  $i$ th and  $j$ th modal frequency respectively.

Notice that when no fluid exists, equation (8) reduces to the usual orthogonality condition  $\mathbf{u}^{(i)} \mathbf{M}_{UU} \mathbf{u}^{(j)} = \delta_{ij}$ .

With modal damping ratio  $\zeta_j$  for the  $j$ th mode, the modal equation of motion can be written as

$$\ddot{x}_j + 2\omega_j \zeta_j \dot{x}_j + \omega_j^2 x_j = -\frac{1}{\omega_j} (\mathbf{F}^{(j)})^T \dot{\mathbf{R}}_\phi + (\mathbf{U}^{(j)})^T \mathbf{R}_u, \quad (9)$$

where the load vectors are

$$\begin{aligned} \mathbf{R}_\phi &= \mathbf{C}_{FU} \mathbf{d}_k \dot{u}_{gk}, \\ \mathbf{R}_u &= -(\mathbf{K}_{UU})_S \mathbf{d}_k u_{gk} - \mathbf{M} \mathbf{d}_k \ddot{u}_{gk}, \end{aligned} \quad (10)$$

hence,

$$\begin{aligned} \ddot{x}_j + 2\omega_j \zeta_j \dot{x}_j + \omega_j^2 x_j &= -\left(\frac{1}{\omega_j} (\mathbf{F}^{(j)})^T \mathbf{C}_{FU} \mathbf{d}_k + (\mathbf{U}^{(j)})^T \mathbf{M} \mathbf{d}_k\right) \ddot{u}_{gk} \\ &\quad - (\mathbf{U}^{(j)})^T (\mathbf{K}_{UU})_S \mathbf{d}_k u_{gk}. \end{aligned} \quad (11)$$

Note that the term  $(\mathbf{K}_{UU})_S$  is numerically very small compared with the rest of the structural stiffness matrix, when there is a structure adjacent to the fluid. Therefore, the term  $(\mathbf{U}^{(j)})^T (\mathbf{K}_{UU})_S \mathbf{d}_k u_{gk}$  can be neglected. Then, equation (11) can be rewritten as

$$\ddot{x}_j + 2\omega_j \zeta_j \dot{x}_j + \omega_j^2 x_j = -\Gamma^{(j)} \ddot{u}_{gk}, \quad (12)$$

where the  $j$ th modal participation factor is

$$\Gamma^{(j)} = \left( \frac{1}{\omega_j} (\mathbf{F}^{(j)})^T \mathbf{C}_{FU} \mathbf{d}_k + (\mathbf{U}^{(j)})^T \mathbf{M} \mathbf{d}_k \right). \quad (13)$$

If the eigenvectors meet the orthogonality condition (7), the  $j$ th modal participation mass  $m_j$  and the accumulated modal participation mass of the first  $n$  modes are

$$\begin{aligned} m_j &= (\Gamma^{(j)})^2, \\ m &= \sum_{j=1}^n m_j = \sum_{j=1}^n (\Gamma^{(j)})^2. \end{aligned} \quad (14)$$

**5.2. Definition of Hydrodynamic Added Mass.** For convenience, two symbols of  $m_x^0$  and  $m_y^0$  are introduced to denote the accumulated modal participation masses along the  $x$ -axis and  $y$ -axis for the hollow pier specimen without water, and accordingly the symbols of  $m_x^w$  and  $m_y^w$  are used for the specimen submerged by different levels of water. So the hydrodynamic added masses can be defined as (HAM)  $\Delta M_x = m_x^w - m_x^0$  and  $\Delta M_y = m_y^w - m_y^0$ . Besides, the symbols of  $m_{xj}^0$  and  $m_{yj}^0$ ,  $j = 1$  and 2, are also introduced to represent the modal participation masses of the first two modes along the  $x$ -axis and  $y$ -axis for the specimen without water. Similarly, the symbols of  $m_{xj}^w$  and  $m_{yj}^w$ ,  $j = 1$  and 2, are defined for the specimen surrounded in different levels of water. So the modal hydrodynamic added masses (MHAMs) can be obtained through  $\Delta m_{xj} = m_{xj}^w - m_{xj}^0$  and  $\Delta m_{yj} = m_{yj}^w - m_{yj}^0$ .

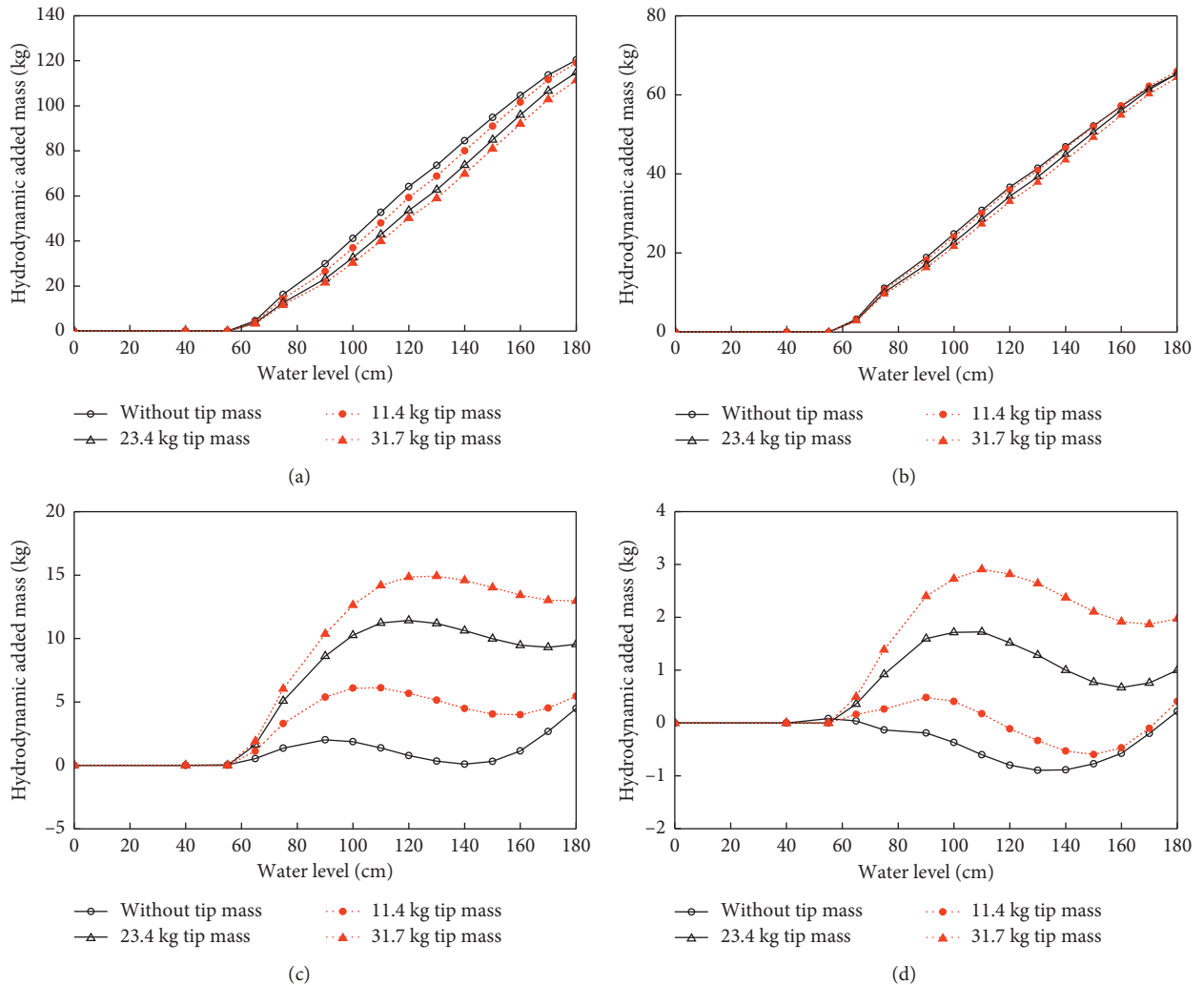
In the finite element code ADINA, the modal participation mass for each vibration mode of a water-structure system can be obtained using the modal participation factor (modal added mass and accumulated added mass) which is provided by ADINA. It is important to point out that the modal analysis should include sufficient numbers of vibration modes to guarantee the accuracy of the accumulated modal participation mass.

**5.3. Effect of Outer Water-Structure Interaction on Hydrodynamic Added Mass.** The HAMs along the  $x$ -axis and  $y$ -axis, respectively, are shown in Table 3 for the specimen with a tip mass equal to 0, 11.4, 23.4, and 31.7 kg, respectively, submerged by outer water to various levels. The HAMs along a specific direction are determined using the first 30 vibration modes along the same direction, since higher modes contribute little to the results. The MHAMs defined previously are depicted in Figure 10 with respect to the water levels for the specimen with a tip mass equal to 0, 11.4, 23.4, and 31.7 kg, respectively.

As indicated in Table 3, both the HAMs along the  $x$ -axis and  $y$ -axis, respectively, increase with water level, and the HAMs along the  $x$ -axis are evidently larger than those along the  $y$ -axis for the same water level. It can be seen in Figure 10 that the MHAMs for the four vibration modes present different trends with different water levels. The MHAMs of

TABLE 3: HAM along the  $x$ -axis and  $y$ -axis for the four tip masses in case I.

Water level (cm)	$\Delta M_x$ (kg)				$\Delta M_y$ (kg)			
	Without tip mass	11.4 kg tip mass	23.4 kg tip mass	31.7 kg tip mass	Without tip mass	11.4 kg tip mass	23.4 kg tip mass	31.7 kg tip mass
40	0	0	0	0	0	0	0	0
55	0	0	0	0	0	0	0	0
65	5.20	5.19	5.20	5.20	3.30	3.30	3.30	3.30
75	17.62	17.60	17.62	17.62	10.97	10.97	10.97	10.97
80	22.19	22.17	22.18	22.19	13.64	13.64	13.64	13.64
90	31.85	31.84	31.84	31.85	18.68	18.68	18.68	18.68
100	43.06	43.04	42.90	42.91	24.48	24.48	24.39	24.39
110	54.17	54.14	54.14	54.14	30.25	30.25	30.25	30.25
120	65.08	65.08	65.04	65.04	35.90	35.90	35.90	35.90
130	74.13	74.14	74.08	74.09	40.57	40.57	40.57	40.57
140	84.82	84.82	84.67	84.67	46.06	46.06	45.98	45.98
150	95.45	95.46	95.41	95.41	51.48	51.48	51.47	51.47
160	106.06	106.07	106.03	106.03	56.86	56.86	56.86	56.86
170	116.67	116.67	116.63	116.63	62.22	62.22	62.22	62.22
180	125.15	125.15	125.10	125.11	66.48	66.48	66.48	66.48
178	125.15	125.15	125.10	125.11	66.48	66.48	66.48	66.48

FIGURE 10: MHAM of the specimen for the four tip masses in case I as a function of water level, corresponding to (a) first mode along the  $x$ -axis; (b) first mode along the  $y$ -axis; (c) second mode along the  $x$ -axis; and (d) second mode along the  $y$ -axis.

the first vibration modes along both directions grow significantly as water level rises, with a maximum value of around 119 kg along the  $x$ -axis and around 62 kg along the  $y$ -axis, and each maximum value is pretty close to the HAM of corresponding direction. The MHAMs of the second vibration modes along both directions display different trends from those of first vibration modes where monotonic increases can no longer be observed, and the values of the MHAM are much smaller for the second vibration modes along both directions.

It is interesting to note that for a specific water level, the tip mass has little effect on the HAM but has a remarkable influence on the MHAM of different vibration modes. The MHAM of the first modes along both directions decrease with the increase of tip mass, whereas the MHAM of the second modes show an opposite trend. Therefore, a conclusion can be deduced that the HAM of the water-surrounded specimen for both directions are closely related to pier dimensions and water level but are of little relevance to the tip mass. It is worthwhile to point out that the curves of the MHAM show a similar tendency to the curves of the vibration period percentage increases as indicated in Figure 6, which further validates the numerical simulations against the obtained experimental data.

**5.4. Effect of Inner Water-Structure Interaction on Hydrodynamic Added Mass.** Table 4 lists the HAMs along the  $x$ -axis and  $y$ -axis, respectively, for the specimen with a tip mass equal to 0, 11.4, 23.4, and 31.7 kg, respectively, interacting with various levels of inner water. The MHAMs of the specimen corresponding to the first two vibration modes along the  $x$ -axis and  $y$ -axis, respectively, are depicted with respect to inner water levels for the four tip masses in Figure 11. For the sake of comparison with case I, the abscissas of the figures still range from 0–180 cm, among which the portion of 0–80 cm corresponds to the results obtained without inner water.

It can be seen in Table 4 that the HAMs for both directions increase with inner water level, and their values are close to each other for a specific level of inner water. As shown in Figure 11, the curves of the MHAM corresponding to the four vibration modes display different trends with different water levels. The curves corresponding to the first vibration mode along both directions ascend monotonically as the inner water height increases, with slightly larger values found along the  $x$ -axis than those along the  $y$ -axis for the same level of inner water. The curves for the second vibration mode along both directions exhibit a bit complicated trend with inner water level, although the variation amplitudes of the curves remain negligibly small. As in case I, the tip mass imposed at the top of the hollow pier plays a similar role in affecting the MHAM induced by inner water in case II. Hence, a similar conclusion can be drawn in case II that the HAMs for both directions of the specimen interacting with inner water have little relevance to the tip mass which is closely related to the MHAM of each vibration mode.

The observations made from Figure 11 are consistent with those from Figure 7, which also provides convincing

validation of the numerical simulations against the obtained experimental data.

**5.5. Effect of Water-Structure Interaction on Vibration Periods Taking into Consideration Both Outer and Inner Water.** Table 5 presents the HAMs of the specimen along the  $x$ -axis and  $y$ -axis, respectively, for the tip masses of 0, 11.4, 23.4, and 31.7 kg, respectively, in case III where the specimen interacts with both outer and inner water. As shown in Figure 12, the MHAMs of the specimen corresponding to the first two vibration modes along the  $x$ -axis and  $y$ -axis, respectively, are plotted with respect to the water levels considered herein for the four tip masses.

As indicated in Table 5 and Figure 12, the variations of the HAM and the MHAM of the specimen in case III show similar trends to those in case I for both directions, with an obvious difference, it was found that noticeably larger values are obtained in case III than in case I. And again, the observations indicated in Figure 12 are consistent with those in Figure 8, and the numerical results are successfully validated against the experimental data.

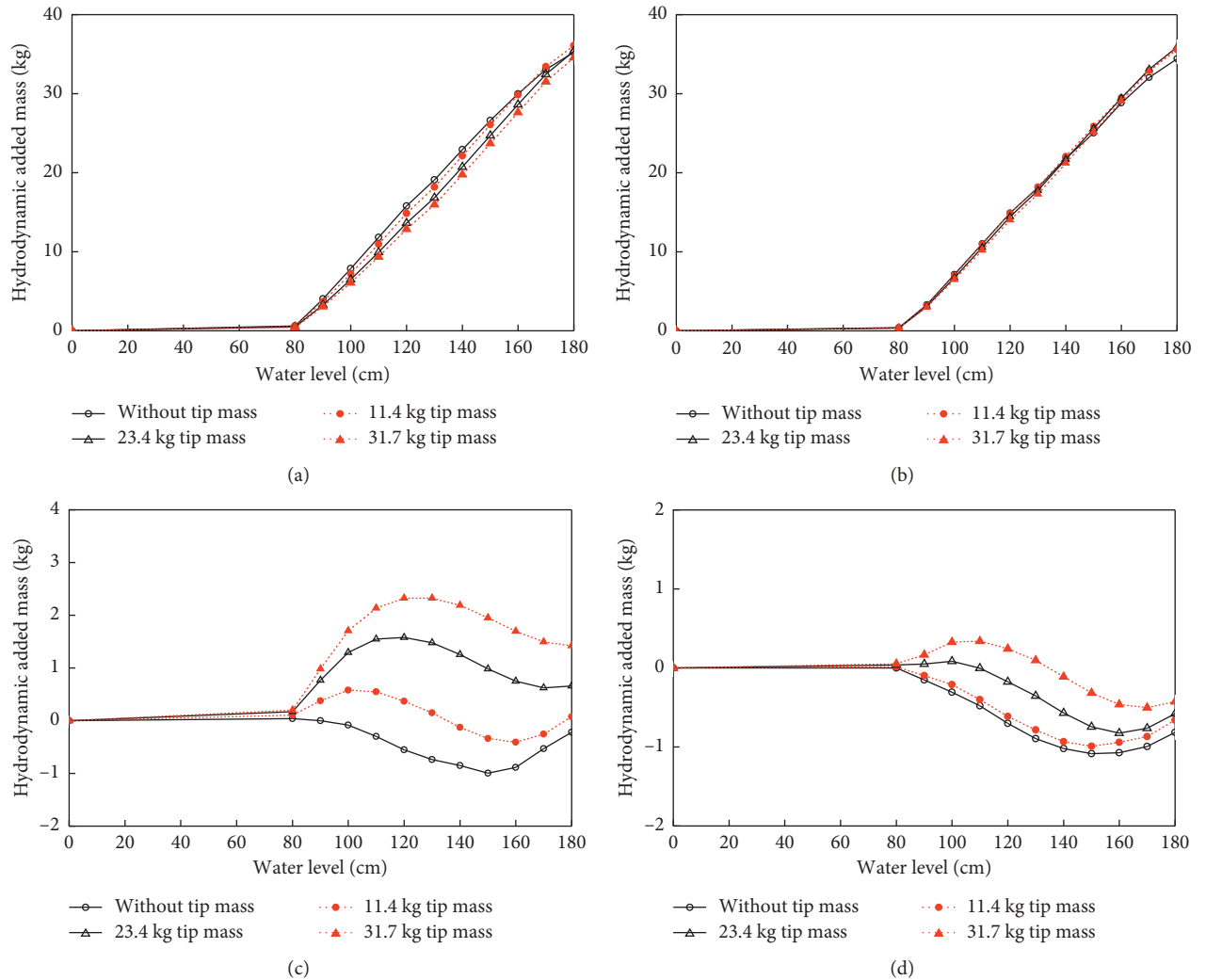
## 6. Equivalent Model Based on Hydrodynamic Added Mass

**6.1. Distribution of Hydrodynamic Added Mass.** This section is intended to discuss the distribution of HAM along the height of the specimen. As indicated in Tables 3 and 5, the HAMs induced by pile-water interaction in various cases are negligibly small, and no HAMs are considered to the piles in the equivalent models to be discussed. Therefore, when  $H_w = 75$  cm, the HAM can be deemed to be induced by cap-water interaction; and when  $H_w > 75$  cm, the HAM consists of two parts: one is induced by cap-water interaction and the other is induced by pier-water interaction. Supposing the HAM induced by cap-water interaction remain constant with the increase of water level ( $H_w > 75$  cm), the HAM to the pile cap and pier body, as shown in Tables 6 and 7, can be readily calculated for various cases using the data presented in Tables 3–5. It can be seen from Tables 6 and 7 that the HAM obtained in case III (taking into consideration both the effects of outer and inner water) approximate the sum of those in case I (taking into consideration only the effect of outer water) and case II (taking into consideration only the effect of inner water) under same analytical or experimental conditions.

The HAMs to the pile cap are assumed to be evenly distributed along the height since the pile caps in the practical engineering are commonly small in height when compared with piers, and the HAM induced by pier-water interaction is distributed along the pier submerged portion according to its actual distribution pattern. Previous researchers pointed out that the HAM at a particular point is proportional to the hydrodynamic pressure on the surface and the acceleration of the structure at that point, which are irrelevant to the vibration shape of the structure [11, 14, 24]. Figures 10–12 reveal that the HAM of the specimen along the  $x$ -axis (or  $y$ -axis) is mainly dependent on the

TABLE 4: HAM along the  $x$ -axis and  $y$ -axis for the four tip masses in case II.

Water level (cm)	$\Delta M_x$ (kg)				$\Delta M_y$ (kg)			
	Without tip mass	11.4 kg tip mass	23.4 kg tip mass	31.7 kg tip mass	Without tip mass	11.4 kg tip mass	23.4 kg tip mass	31.7 kg tip mass
80	0.66	0.66	0.66	0.66	0.40	0.40	0.40	0.40
90	4.06	4.06	4.06	4.06	3.17	3.17	3.17	3.17
100	7.82	7.82	7.82	7.82	6.83	6.83	6.83	6.83
110	11.58	11.57	11.57	11.57	10.57	10.57	10.57	10.57
120	15.32	15.32	15.32	15.32	14.32	14.32	14.32	14.32
130	18.48	18.48	18.48	18.48	17.47	17.47	17.47	17.47
140	22.22	22.21	22.17	22.17	21.21	21.21	21.21	21.21
150	25.99	25.98	25.95	25.95	24.98	24.97	24.97	24.97
160	29.73	29.72	29.68	29.68	28.72	28.72	28.72	28.72
170	33.48	33.47	33.43	33.44	32.47	32.47	32.47	32.47
180	36.47	36.46	36.43	36.43	35.47	35.47	35.47	35.47

FIGURE 11: MHAM of the specimen for the four tip masses in case II as a function of water level, corresponding to (a) first mode along the  $x$ -axis; (b) first mode along the  $y$ -axis; (c) second mode along the  $x$ -axis; and (d) second mode along the  $y$ -axis.

contributions of the fundamental vibration mode along the same direction. Hence, the hydrodynamic pressure and the modal acceleration in the fundamental mode are utilized to obtain the distribution of the HAM along the specimen.

Figures 13 and 14 present the relative accelerations distribution, the relative hydrodynamic pressures distribution, and the relative HAM distribution for the first vibration modes along the  $x$ -axis and  $y$ -axis of the specimen without

TABLE 5: HAM along the  $x$ -axis and  $y$ -axis for the four tip masses in case III.

Water level (cm)	$\Delta M_x$ (kg)				$\Delta M_y$ (kg)			
	Without tip mass	11.4 kg tip mass	23.4 kg tip mass	31.7 kg tip mass	Without tip mass	11.4 kg tip mass	23.4 kg tip mass	31.7 kg tip mass
40	0.00	0.00	0.00	0.00	0.00	0.00	0.00	0.00
55	0.00	0.00	0.00	0.00	0.00	0.00	0.00	0.00
65	5.20	5.19	5.20	5.20	3.30	3.30	3.30	3.30
75	17.62	17.60	17.62	17.62	10.97	10.97	10.97	10.97
80	22.84	22.83	22.84	22.85	14.05	14.05	14.05	14.05
90	35.91	35.90	35.90	35.92	21.85	21.85	21.85	21.85
100	50.88	50.85	50.86	50.86	31.31	31.31	31.31	31.31
110	65.74	65.74	65.70	65.71	40.82	40.82	40.82	40.82
120	80.40	80.40	80.35	80.35	50.22	50.22	50.22	50.22
130	92.63	92.63	92.56	92.55	58.05	58.05	58.04	58.04
140	107.07	107.05	106.96	106.95	67.28	67.28	67.25	67.25
150	121.45	121.44	121.37	121.37	76.46	76.46	76.44	76.44
160	135.81	135.79	135.74	135.75	85.59	85.59	85.59	85.59
170	150.15	150.08	150.08	150.09	94.69	94.69	94.69	94.69
180	161.63	161.56	161.56	161.56	101.95	101.95	101.95	101.95

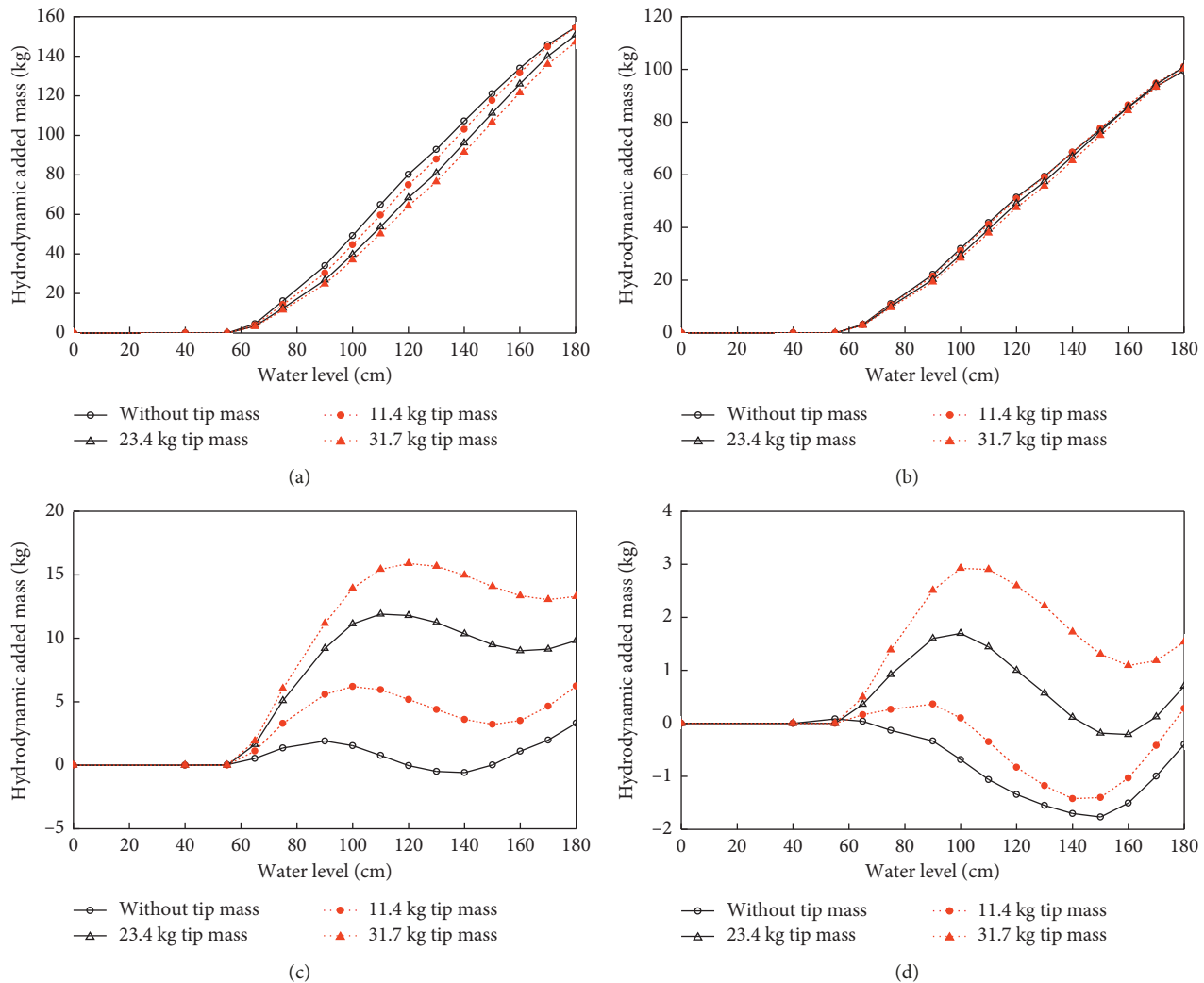
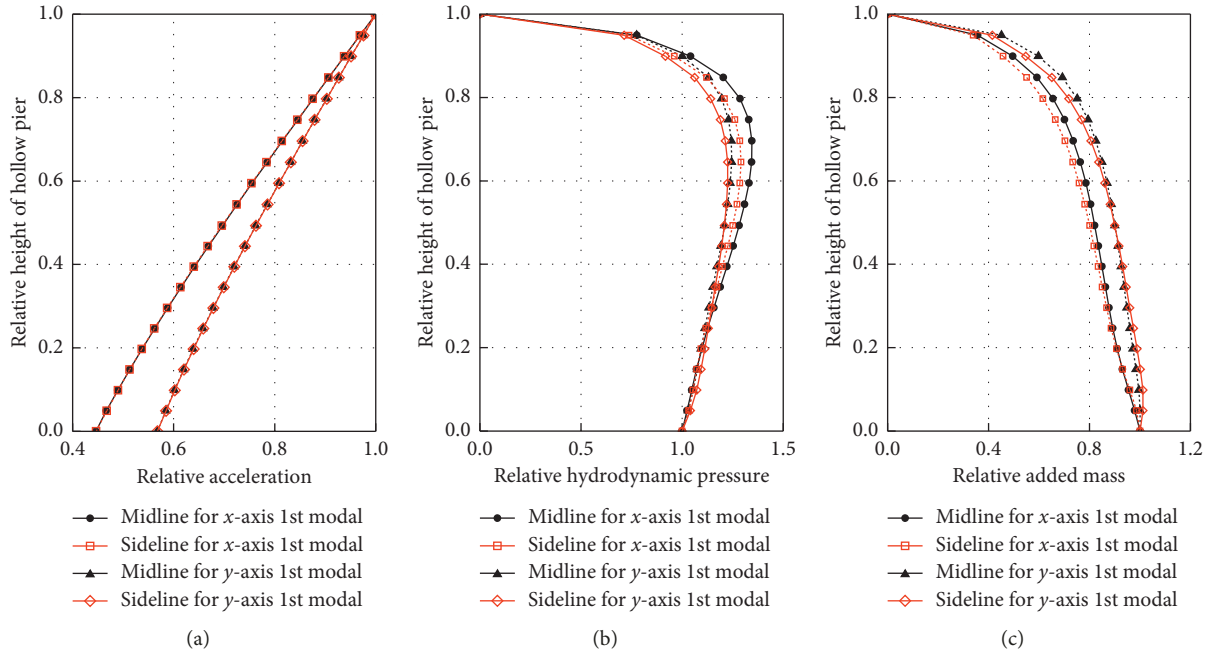
FIGURE 12: MHAM of the specimen for the four tip masses in case III as a function of water level, corresponding to (a) first mode along the  $x$ -axis; (b) first mode along the  $y$ -axis; (c) second mode along the  $x$ -axis; and (d) second mode along the  $y$ -axis.

TABLE 6: HAM of the pile cap along the  $x$ -axis and  $y$ -axis in the three cases.

Water level (cm)	$\Delta M_x$ (kg)			$\Delta M_y$ (kg)		
	Case I	Case II	Case III	Case I	Case II	Case III
75–180	17.62	0	17.62	10.97	0	10.97

TABLE 7: HAM of the pier along the  $x$ -axis and  $y$ -axis in the three cases.

Water level (cm)	$\Delta M_x$ (kg)					$\Delta M_y$ (kg)				
	Case I (1)	Case II (2)	(1) + (2)(3)	Case III (4)	(3)/(4)	Case I (5)	Case II (6)	(5) + (6)(7)	Case III (8)	(7)/(8)
80	4.57	0.66	5.23	5.22	1.00	2.68	0.40	3.08	3.080	1.00
90	14.23	4.06	18.29	18.30	1.00	7.71	3.17	10.88	10.881	1.00
100	25.44	7.82	33.26	33.258	1.00	13.51	6.83	20.34	20.343	1.00
110	36.55	11.58	48.13	48.12	1.00	19.28	10.57	29.85	29.853	1.00
120	47.46	15.32	62.78	62.78	1.00	24.93	14.32	39.25	39.250	1.00
130	56.51	18.48	74.99	75.01	1.00	29.60	17.47	47.07	47.085	1.00
140	67.20	22.22	89.42	89.45	1.00	35.09	21.21	56.30	56.315	1.00
150	77.83	25.99	103.82	103.83	1.00	40.51	24.98	65.49	65.488	1.00
160	88.45	29.73	118.18	118.19	1.00	45.90	28.72	74.62	74.618	1.00
170	99.05	33.48	132.53	132.53	1.00	51.25	32.47	83.72	83.719	1.00
180	107.53	36.47	144.00	144.01	1.00	55.51	35.47	90.98	90.981	1.00

FIGURE 13: Distribution of relative modal acceleration, relative hydrodynamic pressure, and relative HAM along the specimen without tip mass corresponding to a water level of  $H_w = 1.8$  m in case I: (a) relative modal acceleration; (b) relative hydrodynamic pressure; (c) relative HAM.

tip mass surrounded by a water level of  $H_w = 1.8$  m in case I and case II, respectively (relative accelerations, relative hydrodynamic pressures, and the relative HAM in Figures 13 and 14 were obtained taking the point in each graph whose ordinate value is 1 as reference point, separately). Two sets of results are given for each figure, and they are corresponding to the middle vertical line and the side vertical line (to refer them hereinafter as mid-line and side-line for short), respectively, on the surface of the pier perpendicular

to the vibration direction. It is evident that the distributions of the HAM obtained using the results along mid-line are consistent with those obtained using the results along side-line in both case I and case II. For convenience, the HAM corresponding to the mid-line is computed for other tip masses and water levels, and typical results are discussed below.

Figures 15 and 16 illustrate the HAM distribution of the specimen with tip masses of 0, 11.4, 23.4, and 31.7 kg,

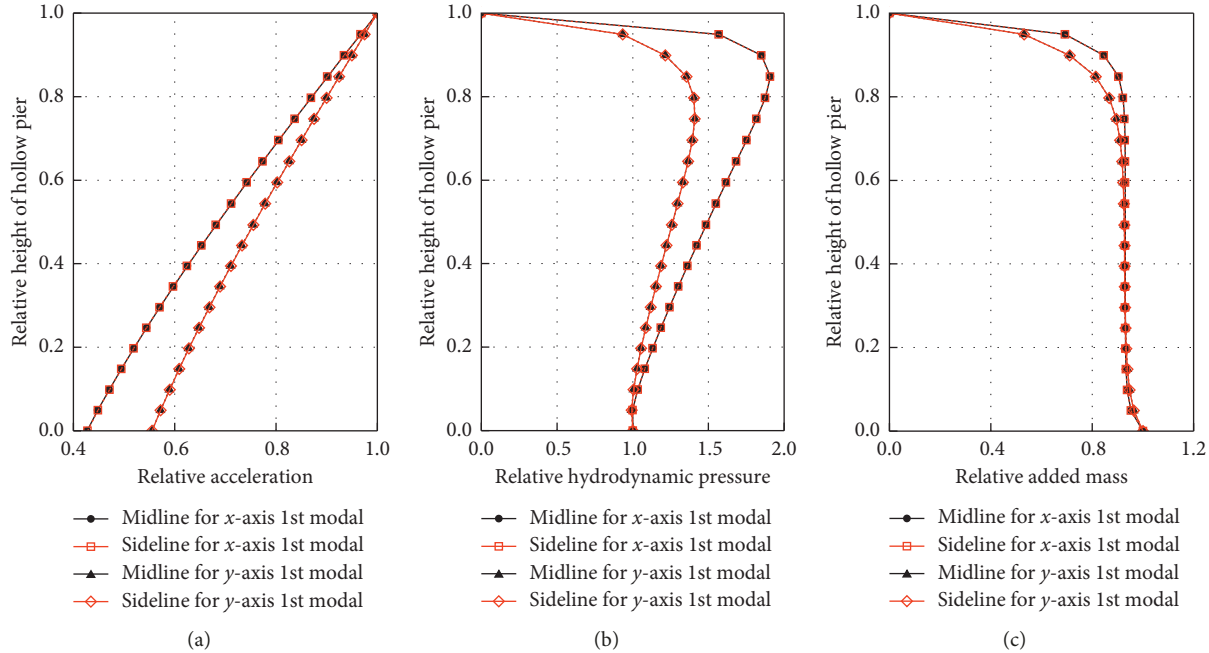


FIGURE 14: Distribution of relative modal acceleration, relative hydrodynamic pressure, and relative HAM along the specimen without tip mass corresponding to a water level of  $H_w = 1.8$  m in case II: (a) relative modal acceleration; (b) relative hydrodynamic pressure; (c) relative HAM.

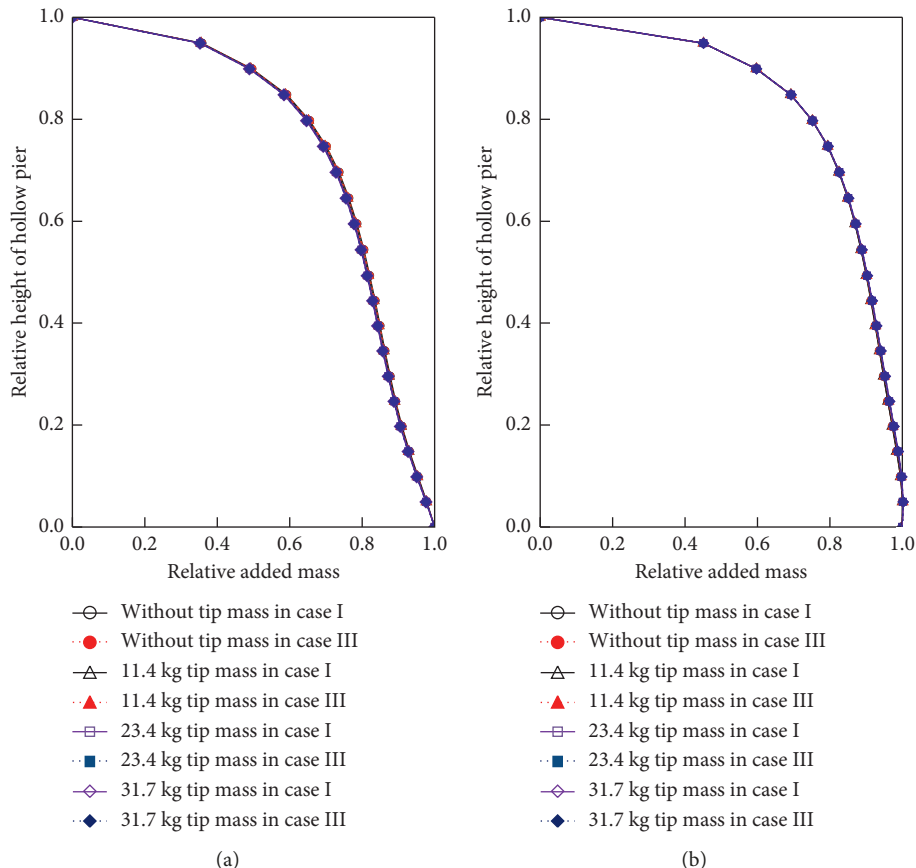


FIGURE 15: Comparison of the relative added mass distributions along the specimen corresponding to a water level of  $H_w = 1.8$  m between: (a) case III and case I along the x-axis; (b) case III and case I along the y-axis.

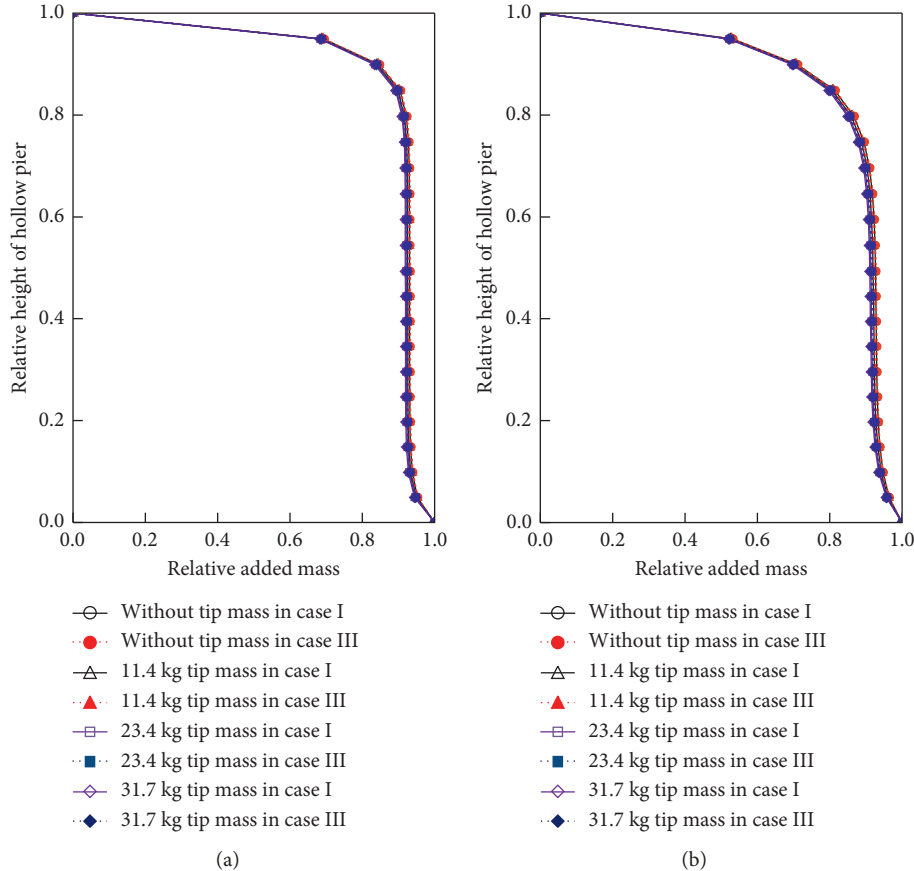


FIGURE 16: Comparison of the relative added mass distributions along the specimen corresponding to a water level of  $H_w = 1.8$  m between: (a) case III and case II along the  $x$ -axis; (b) case III and case II along the  $y$ -axis.

respectively, corresponding to a water level of  $H_w = 1.8$  m in different cases. It is shown that the tip mass has little effect on the magnitude or distribution of the HAM along the specimen. This observation can also be made from the results corresponding to other water levels (for brevity, they are not detailed herein).

**6.2. Equivalent Models.** The assumption that the HAMs are uniformly distributed along the structure submerged by water [8, 9, 11] is applied to established Equivalent model I of the specimen. Meanwhile, the distributions of the HAM along the specimen, discussed in Section 6.1, are also applied and incorporated into a finite element model of the specimen which is denoted as Equivalent model II. In order to provide reasonable comparisons, the modeling details of piles, pile cap, and hollow pier body remain the same as elaborated in Section 3.2. The HAMs are modeled through modified material density in Equivalent model I and through distributed added masses directly to the nodes in Equivalent model II, as illustrated in Figure 17.

*6.3. Comparison of Vibration Periods.* The symbols  $\tilde{T}_{xj}^w$  and  $\tilde{T}_{yj}^w$ ,  $j = 1, 2$ , are introduced to represent the vibration periods of the two equivalent models along the  $x$ -axis and  $y$ -axis,

respectively, with the subscript  $j = 1$  representing Equivalent model I and the subscript  $j = 2$  representing Equivalent model II. The vibration periods  $T_{xj}^w, j = 1, 2$  and  $T_{yj}^w, j = 1, 2$  are obtained using the FEM established in Section 3.2, corresponding to the first two vibration modes along the  $x$ -axis and  $y$ -axis, respectively. So, the vibration period ratios  $R_{xj} = \tilde{T}_{xj}^w/T_{xj}^w$  and  $R_{yj} = \tilde{T}_{yj}^w/T_{yj}^w, j = 1, 2$ , are defined to discuss the application of the two equivalent models.

The vibration period ratios of the first two modes along the  $x$ -axis and  $y$ -axis, respectively, are plotted against water level as shown in Figures 18–20, corresponding to case I, case II, and case III. In Figures 18–20, the results of the specimen with four tip masses of 0, 11.4, 23.4, and 31.7 kg, are included corresponding to water levels not lower than  $H_w = 0.8$  m, since the pier body cannot contact water if lower water levels are considered in analysis (Figure 4). As illustrated in Figure 18, convincing agreement can be reached between the results obtained by Equivalent model II and the FEM mentioned in Section 3.2, with a maximum error smaller than 1% provided the results of the FEM are exact, comparing with a maximum error of 3.1% caused by Equivalent model I. Similar conclusions can also be drawn from Figure 20. However, in case II, as seen in Figure 19, the results of Equivalent model I and Equivalent model II are all fit to those of the FEM well with both maximum errors no more

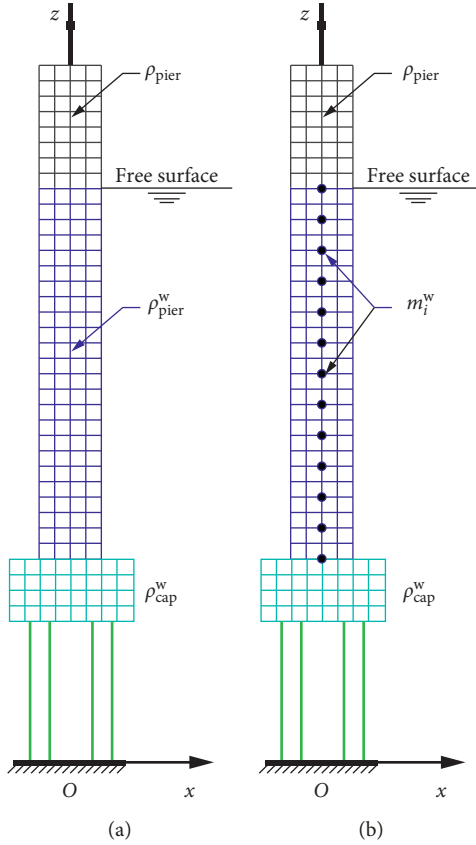


FIGURE 17: Two equivalent models considered: (a) Equivalent model I; (b) Equivalent model II.

than 0.6%, while Equivalent model II displays better agreement with the FEM.

It can be drawn from above discussions that it is not always appropriate to assume a uniform distribution of hydrodynamic added masses in performing simplified analysis of fluid-structure interaction. For the hollow pier specimen, the HAM induced by outer water should be distributed along the submerged portion in its practical distribution pattern, but the HAM induced by inner water can still be taken to be uniformly distributed along the submerged portion. The distribution of HAM considering both the effects of outer and inner water is approximately the superposition of those considering only the effect of outer and inner water, respectively. It is also important to note that the conclusions herein might only be applicable to the hollow pier specimen considered in this paper and should not be extrapolated directly to seismic or other dynamic load response analyses of structures surrounded by water.

## 7. Summary and Conclusions

This paper presents an experiment program conducted to study the modal dynamic response of hollow bridge pier with pile group foundation submerged in water. A reduced scale hollow pier was designed and tested in three cases where the specimen contacts with only outer water, only inner water, and both outer and inner water, respectively. Four tip masses, that is, 0, 11.4, 23.4, 31.7 kg, were

considered in the tests to present the effect of bridge superstructure mass. Various water levels were defined as a function in the tests. Three-dimensional finite element models, corresponding to the specimen tested under combination conditions of the three cases, the four tip masses, and various water levels mentioned above, were established. The vibration periods of the first four lateral modes, including the first two modes along the  $x$ -axis and the first two modes along the  $y$ -axis, were measured and calculated. The experimental results and the numerical results were then validated against each other. Based on the validated models, the hydrodynamic added masses were calculated and analyzed. An equivalent model (Equivalent model II) was proposed based on the hydrodynamic added mass distribution which was obtained by using the hydrodynamic pressure and the modal acceleration. Equivalent model I was also established through uniform distribution of the hydrodynamic added mass. Vibration periods of Equivalent model I and Equivalent model II were calculated and compared. The following conclusions can be made based on this research:

- (1) In the three cases that structure contacts with only outer water, only inner water and both outer, and inner water, the vibration periods of the hollow pier specimen increases as water level rises, indicating the effect of fluid-structure interaction on the modal response of the specimen increases with water level. Among the three cases, the effect of fluid-structure

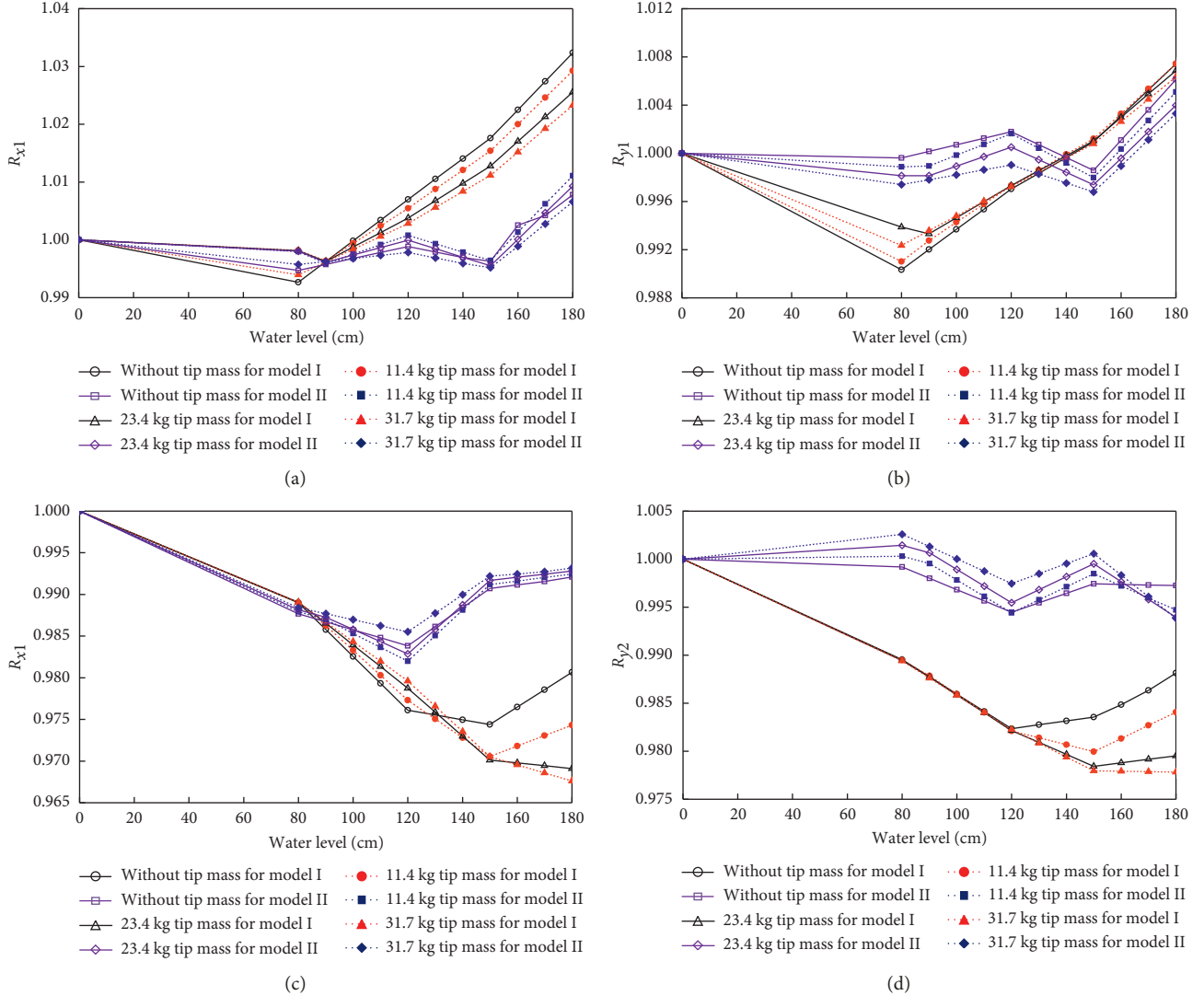


FIGURE 18: Vibration period ratios of the specimen in case I as a function of water level correspond to (a) first mode along the  $x$ -axis; (b) first mode along the  $y$ -axis; (c) second mode along the  $x$ -axis; and (d) second mode along the  $y$ -axis.

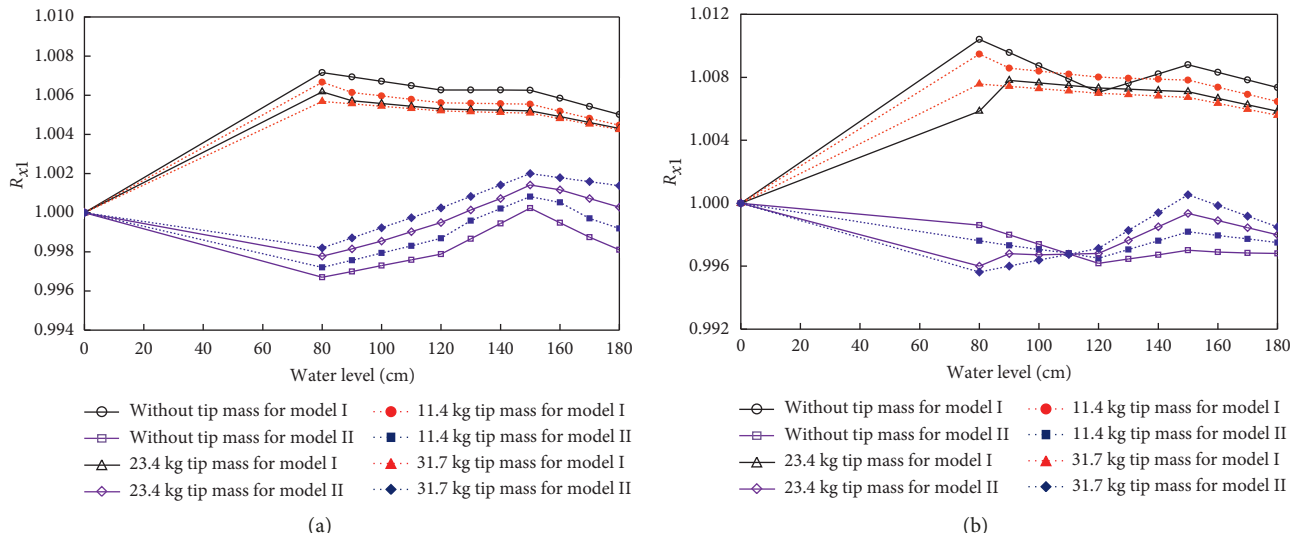


FIGURE 19: Continued.

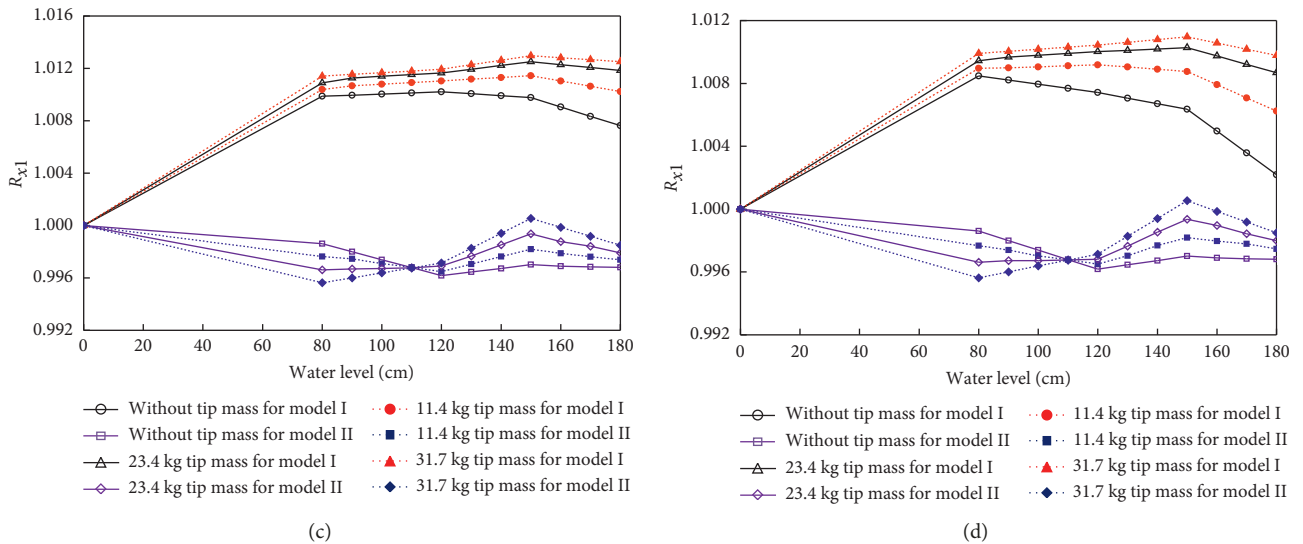


FIGURE 19: Vibration period ratios of the specimen in case II as a function of water level correspond to: (a) first mode along the  $x$ -axis; (b) first mode along the  $y$ -axis; (c) second mode along the  $x$ -axis; and (d) second mode along the  $y$ -axis.

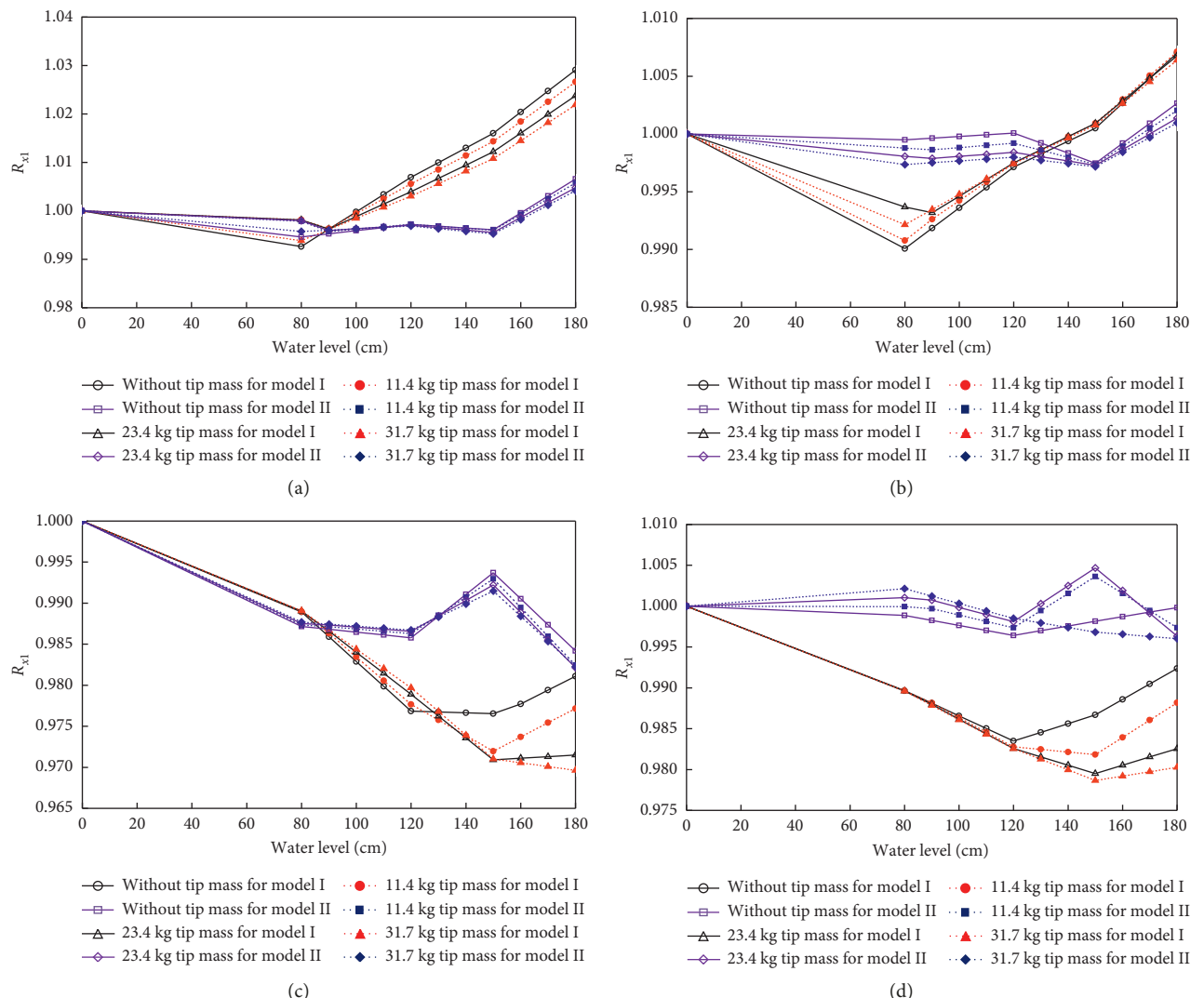


FIGURE 20: Vibration period ratios of the specimen in case III as a function of water level correspond to: (a) first mode along the  $x$ -axis; (b) first mode along the  $y$ -axis; (c) second mode along the  $x$ -axis; and (d) second mode along the  $y$ -axis.

- interaction is largest when both outer and inner water are considered and is smallest when only inner water is taken into consideration.
- (2) In each of the three cases, the vibration period percentage increases of the hollow pier specimen increase monotonically with water level for the first modes along both the  $x$ -axis and  $y$ -axis and show a complicated fashion with water level for the second modes along both the  $x$ -axis and  $y$ -axis. Generally, the vibration period percentage increases for the second modes are large when water level is lower than the mid-height of the pier and are much smaller when water level is over the mid-height of the pier.
  - (3) When the structure couples with outer water or both inner and outer water, the vibration period percentage increases of the modes along the  $x$ -axis are evidently higher than those along the  $y$ -axis; the result is caused by the fact that the area of fluid-structure potential interfaces perpendicular to the  $x$ -axis is larger than that perpendicular to the  $y$ -axis. When the structure couples with only inner water, however, the vibration period percentage increases are comparable along the  $x$ -axis and  $y$ -axis.
  - (4) In all the three cases, the vibration period percentage increases of the hollow pier specimen decrease with tip mass for the first modes along both the  $x$ -axis and  $y$ -axis and increase significantly with tip mass for the second modes along both the  $x$ -axis and  $y$ -axis.
  - (5) In the case where structure contacts with only outer water or both outer and inner water, the hydrodynamic added masses induced by pile-water interactions are negligibly small and the major contribution to the hydrodynamic added masses comes from hollow pier body-water interaction. The hydrodynamic added masses considering both the effects of outer and inner water are approximately the sum of those considering only the effect of outer and inner water, respectively.
  - (6) In all the three cases, the tip mass has little effect on the magnitudes of the hydrodynamic added masses, but has a remarkable impact on the modal hydrodynamic added masses.
  - (7) The Equivalent model II put forward in the manuscript is reliable for its more accuracy when compared with Equivalent model I. And, for the hollow pier specimen considered in this paper, the hydrodynamic added masses induced by outer water are inadvisable to be simply taken as uniform distribution along the submerged portion; its practical distribution pattern is better, while those induced by inner water could be assumed to be distributed uniformly along the submerged portion since the errors of these two equivalent models are close to each other.
- ## Data Availability
- The data used to support the findings of this study are available from the corresponding author upon request.
- ## Disclosure
- Any opinions, findings, and conclusions expressed herein are those of the authors and do not necessarily reflect the views of the sponsors.
- ## Conflicts of Interest
- The authors declare that they have no conflicts of interest.
- ## Acknowledgments
- This work was supported by the National Nature Science Foundation of China (Grant nos. 51678459 and 51378406) and Chongqing Research Program of Basic Research and Frontier Technology (Grant no. cstc2015jcyjA30014). The authors are very grateful for the supports.
- ## References
- [1] W. P. Yen, G. Chen, M. Yashinski et al., "Lessons in bridge damage learned from the Wenchuan earthquake," *Earthquake Engineering and Engineering Vibration*, vol. 8, no. 2, pp. 275–285, 2009.
  - [2] W. H. P. Yen, G. D. Chen, M. Yashinsky et al., "China earthquake reconnaissance report: performance of transportation structures during the May 12, 2008, M7.9 Wenchuan earthquake," Rep. No. FHWA-HRT-11-029, Federal Highway Administration, Washington, DC, USA, 2011.
  - [3] R. B. Bittner, X. G. Zhang, and O. J. Jensen, "Design and construction of the Sutong bridge foundations," *DFI Journal-The Journal of Deep Foundations Institute*, vol. 1, no. 1, pp. 2–18, 2007.
  - [4] Q. You, P. He, X. Dong, X. Zhang, and S. Wu, "Sutong bridge—the longest cable-stayed bridge in the world," *Structural Engineering International*, vol. 18, no. 4, pp. 390–395, 2018.
  - [5] S.-x. Liu, Y.-c. Li, and G.-w. Li, "Wave current forces on the pile group of base foundation for the east sea bridge, China," *Journal of Hydrodynamics*, vol. 19, no. 6, pp. 661–670, 2007.
  - [6] K. Hiroshi, "Evaluation of wave force acting on submerged floating tunnels," *Procedia Engineering*, vol. 4, pp. 99–105, 2010.
  - [7] J. F. Manwell, C. N. Elkinton, A. L. Rogers, and J. G. McGowan, "Review of design conditions applicable to offshore wind energy systems in the United States," *Renewable and Sustainable Energy Reviews*, vol. 11, no. 2, pp. 210–234, 2007.
  - [8] J. R. McGowan, J. W. Johnson, S. A. Schaaf et al., "The force exerted by surface waves on piles," *Journal of Petroleum Technology*, vol. 2, no. 5, pp. 149–154, 2013.
  - [9] J. Penzien and M. K. Kaul, "Response of offshore towers to strong motion earthquakes," *Earthquake Engineering and Structural Dynamics*, vol. 1, no. 1, pp. 55–68, 1972.
  - [10] T. Sarpkaya, "Force on a circular cylinder in viscous oscillatory flow at low Keulegan-Carpenter numbers," *Journal of Fluid Mechanics*, vol. 165, no. 1, pp. 61–71, 2006.
  - [11] W. Yang and Q. Li, "The expanded Morison equation considering inner and outer water hydrodynamic pressure of hollow piers," *Ocean Engineering*, vol. 69, pp. 79–87, 2013.
  - [12] X. Du, P. Wang, and M. Zhao, "Simplified formula of hydrodynamic pressure on circular bridge piers in the time domain," *Ocean Engineering*, vol. 85, pp. 44–53, 2014.
  - [13] A. Goyal and A. K. Chopra, "Earthquake analysis of intake-outlet towers including tower-water-foundation-soil

- interaction," *Earthquake Engineering and Structural Dynamics*, vol. 18, no. 3, pp. 325–344, 1989.
- [14] C.-Y. Liaw and A. K. Chopra, "Dynamics of towers surrounded by water," *Earthquake Engineering and Structural Dynamics*, vol. 3, no. 1, pp. 33–49, 1974.
- [15] J. T. Xing, W. G. Price, M. J. Pomfret, and L. H. Yam, "Natural vibration of a beam-water interaction system," *Journal of Sound and Vibration*, vol. 199, no. 3, pp. 491–512, 1997.
- [16] N. Bouaanani and F. Y. Lu, "Assessment of potential-based fluid finite elements for seismic analysis of dam-reservoir systems," *Computers and Structures*, vol. 87, no. 3-4, pp. 206–224, 2009.
- [17] M. Di Pilato, F. Perotti, and P. Fogazzi, "3D dynamic response of submerged floating tunnels under seismic and hydrodynamic excitation," *Engineering Structures*, vol. 30, no. 1, pp. 268–281, 2008.
- [18] G. C. Everstine, "A symmetric potential formulation for fluid-structure interaction," *Journal of Sound and Vibration*, vol. 79, no. 1, pp. 157–160, 1981.
- [19] L. G. Olson and K. J. Bathe, "An infinite element for analysis of transient fluid-structure interactions," *Engineering Computations*, vol. 2, no. 4, pp. 319–329, 1985.
- [20] K. Wei, W. Yuan, and N. Bouaanani, "Experimental and numerical assessment of the three-dimensional modal dynamic response of bridge pile foundations submerged in water," *Journal of Bridge Engineering*, vol. 18, no. 10, pp. 1032–1041, 2013.
- [21] K. Wei, N. Bouaanani, and W. Yuan, "Simplified methods for efficient seismic design and analysis of water-surrounded composite axisymmetric structures," *Ocean Engineering*, vol. 104, pp. 617–638, 2015.
- [22] C. H. Zhang, *Numerical Modeling of Concrete Dam-Foundation Reservoir Systems*, Tsinghua University Press, Beijing, China, 2001.
- [23] H. Goto and K. Toki, "Vibration characteristics and aseismic design of submerged bridge piers," in *Proceedings of 3rd World Conference on Earthquake Engineering*, pp. 107–125, Auckland and Wellington, New Zealand, March 1965.
- [24] M. R. Maher and R. T. Severn, "Experimental added-mass in modal vibration of cylindrical structures," *Engineering Structures*, vol. 14, no. 3, pp. 163–175, 1992.
- [25] F. G. Mitri, "Theoretical and experimental determination of the acoustic radiation force acting on an elastic cylinder in a plane progressive wave-far field derivation approach," *New Journal of Physics*, vol. 8, no. 8, pp. 1–14, 2006.
- [26] N. G. Pegg, "An experimental study of the seismic forces on submerged structures," Dissertation, University of Britain, Vancouver, BC, Canada, 1983.
- [27] J.-S. Wu and S.-H. Hsu, "A unified approach for the free vibration analysis of an elastically supported immersed uniform beam carrying an eccentric tip mass with rotary inertia," *Journal of Sound and Vibration*, vol. 291, no. 3–5, pp. 1122–1147, 2006.
- [28] Ministry of Communications of China, "Chinese General Code for Design of Highway Bridges and Culverts (JTG D60-2004)," Ministry of Communications of China, China, 2004.
- [29] Ministry of Communications of China, "Chinese General Code for Design of Highway Bridges and Culverts (JTG D60-2015)," Ministry of Communications of China, China, 2015.
- [30] Y. L. Deng, Q. K. Guo, and L. Q. Xu, "Experimental and numerical study on modal dynamic response of water-surrounded slender bridge pier with pile foundation," *Shock and Vibration*, vol. 2017, Article ID 4769637, 20 pages, 2017.
- [31] ADINA, "ADINA theory and modeling guide," ARD 13-8, Adina R & D Inc., Watertown, MA, USA, 2013.
- [32] W. Lai, J. J. Wang, and S. D. Hu, "Earthquake induced hydrodynamic pressure on bridge pier," *Journal of Tongji Medical University*, vol. 32, no. 1, pp. 1–5, 2004.
- [33] J.-F. Sigrist and S. Garreau, "Dynamic analysis of fluid-structure interaction problems with modal methods using pressure-based fluid finite elements," *Finite Elements in Analysis and Design*, vol. 43, no. 4, pp. 287–300, 2007.

